

**Department of Physics and Astronomy  
University of Heidelberg**

Bachelor Thesis in Physics  
submitted by

**Sarah Lisa Görlitz**

born in Boston, Massachusetts (USA)

**2020**

**Impact of initial conditions on integrated particle yields from Pb-Pb collisions at  $\sqrt{s_{NN}} = 2.76$  TeV and 5.02 TeV**

This Bachelor Thesis has been carried out by Sarah L. Görlitz at the  
Physikalisches Institut in Heidelberg  
under the supervision of  
Prof. Dr. Silvia Masciocchi

# Abstract

This thesis presents a study on the impact of initial conditions on  $p_T$ -integrated particle yields in Pb-Pb collisions. The initial conditions are provided by the T<sub>R</sub>ENTo model for simulations of the QGP's dynamic evolution in heavy-ion collisions with the FluiduM+ FastReso package, which describe the evolution in terms of relativistic hydrodynamics. The initial condition model T<sub>R</sub>ENTo couples a Monte Carlo Glauber approach to an entropy-production mechanism based on the mean of the fluctuated thickness functions of the colliding nuclei. The entropy deposition in the transverse plane is proportional to the mean of the fluctuated thickness functions of the nuclei which is quantified by the parameter  $p$ .

The study is done for Pb-Pb collisions at  $\sqrt{s_{NN}} = 2.76$  TeV and 5.02 TeV by a model-to-data comparison of  $p_T$ -integrated particle yields of all charged particles, kaons and protons of ALICE data and FluiduM results. The latter were calculated with initial conditions for  $p = -0.05, 0, 0.01, 0.05, 0.1, 0.2$  and 0.5. For  $\sqrt{s_{NN}} = 2.76$  TeV, judged by a linear fit to the model-to-data ratios for kaons,  $p = 0 \pm 0.05$  was determined as an optimal range where ALICE data and model calculations agree within the uncertainties. For  $\sqrt{s_{NN}} = 5.02$  TeV only preliminary predictions can be presented here.

# Zusammenfassung

Diese Arbeit befasst sich mit dem Einfluss von Anfangsfeldverteilungen auf die gemessene Multiplizität verschiedener Hadronen bei relativistischen Pb-Pb Kollisionen. Anhand des T<sub>R</sub>ENTo Modells wird die Parametrisierung des Entropiedichteprofiles in der transversalen Ebene untersucht. Die Bestimmung der Entropiedichte zum Zeitpunkt der Bildung des Quark-Gluonen Plasmas ist ein essentieller Input für numerische Simulationen wie dem FluiduM + FastReso Code, welcher die Dynamik des QGP's mittels relativistischer Hydrodynamik beschreibt. Das T<sub>R</sub>ENTo-Modell basiert auf einem Monte Carlo Glauber Ansatz gekoppelt an einen Mechanismus zur Entropie-Produktion. Hierzu werden die transversalen fluktuierenden Nukleondichten der kollidierenden Ionen entsprechend dem Parameter  $p$  gemittelt. Dieser Mittelwert weist eine Proportionalität zur Entropiedichte in der transversalen Ebene auf. Für Blei Kollisionen bei  $\sqrt{s_{NN}} = 2.76$  TeV und 5.02 TeV wurde die Anzahl der Teilchen pro Rapiditätseinheit für geladene Teilchen allgemein, sowie Pionen, Kaonen und Protonen für das Rapiditätsintervall  $|y| < 0.5$  mit FluiduM berechnet und mit ALICE Daten verglichen. Für die theoretischen Berechnungen wurden hierzu Entropiedichte-Profile für  $p = -0.05, 0, 0.01, 0.05, 0.1, 0.2$  und  $0.5$  in T<sub>R</sub>ENTo berechnet. Für  $\sqrt{s_{NN}} = 2.76$  TeV wurde, basierend auf dem Fit des Quotienten aus berechnetem und gemessenem Wert für Kaonen, festgestellt, dass in einem Bereich von  $p = 0 \pm 0.05$  ALICE Daten sowie das Modell innerhalb der Fehler gut übereinstimmen. Dieser Bereich kann aber nicht weiter eingeschränkt werden. Für  $\sqrt{s_{NN}} = 5.02$  TeV werden vorläufige Voraussagen präsentiert.

# Contents

<b>1</b>	<b>Introduction</b>	<b>1</b>
<b>2</b>	<b>Heavy-Ion-Physics and the QGP</b>	<b>2</b>
2.1	Standard Model, Quarks and QCD . . . . .	2
2.2	QGP in Heavy-Ion Collisions . . . . .	5
2.2.1	Evolution in Space-Time . . . . .	6
2.2.2	Flow . . . . .	8
<b>3</b>	<b>Kinematics in Relativistic Collisions</b>	<b>10</b>
3.1	Collision Geometry . . . . .	10
3.1.1	Coordinate System . . . . .	10
3.1.2	Experimental observables . . . . .	11
3.1.3	Event centrality . . . . .	11
3.1.4	Main quantities . . . . .	12
<b>4</b>	<b>Initial State description</b>	<b>14</b>
4.1	About Initial Conditions . . . . .	14
4.2	The Glauber model . . . . .	14
4.2.1	Background information . . . . .	15
4.2.2	Analytical calculations within the Glauber Model . . . . .	15
4.2.3	Monte Carlo Glauber Approach . . . . .	17
4.3	Trento . . . . .	17
4.3.1	Algorithm . . . . .	17
4.3.2	Brief description of the code . . . . .	20
<b>5</b>	<b>Analysis Methods</b>	<b>22</b>
5.1	Outline of the analysis . . . . .	22
5.2	Initial conditions . . . . .	22
5.2.1	Implementation . . . . .	22
5.3	Hydrodynamic evolution and Resonance decays . . . . .	25

5.4	Verification of the setup . . . . .	27
<b>6</b>	<b>Systematic study of T<sub>R</sub>ENTo initial conditions for Pb-Pb collisions at <math>\sqrt{s_{NN}} = 2.76</math> TeV and 5.02 TeV</b>	<b>31</b>
6.1	Motivation . . . . .	31
6.2	Experimental data and uncertainties . . . . .	32
6.3	Fits and Results . . . . .	35
6.3.1	Analysis and Fits . . . . .	35
6.3.2	Fit results: Pb-Pb collisions at $\sqrt{s_{NN}} = 2.76$ TeV . . . . .	36
6.3.3	Comparison of results: Pb-Pb collisions at $\sqrt{s_{NN}} = 5.02$ TeV . . . . .	44
6.3.4	Bugs in the code and possible error sources . . . . .	47
6.4	Open questions and further steps . . . . .	47
<b>7</b>	<b>Conclusion and Outlook</b>	<b>49</b>

# Chapter 1

## Introduction

The heavy-ion program at the **L**arge **H**adron Collider operated by the European Organization of Nuclear Research (CERN) provides a unique opportunity to study the strongly interacting deconfined matter of quarks and gluons, which is known as **q**uark-**g**luon **p**lasma (QGP), that is produced in relativistic heavy-ion collisions. Therefore one of the four large experiments at the collider ring, **A** **L**arge **I**on **C**ollider **E**xperiment (ALICE), is dedicated to the study of properties of this 'new' state. Since the interactions are predominately strong, studies of heavy-ion collisions at ALICE can improve our understanding of **Q**uantum **C**hromo **D**ynamics (QCD), the field theory of the strong interaction, at high temperatures [1]. While nowadays the description of the evolution of the QGP in terms of viscous relativistic hydrodynamics is well understood, numerical schemes that simulate the dynamics of the QGP require an accurate description of the initial entropy (or energy) density distribution in the transverse plane at the time of the QGP's thermalization.

In this thesis, the study the initial field description provided by the initial condition model T<sub>R</sub>ENTo for the numerical hydrodynamic simulation with the FluiduM package (introduced here [2]) and the impact of varying this description on the FluiduM output. In order to do so, the  $p_T$ -integrated particle yields at mid-rapidity measured by ALICE are compared to calculations of the same observable with FluiduM for different parametrizations of initial conditions.

The basic concepts of heavy-ion collisions and the quark-gluon plasma are introduced in **Chapter 2** and **3**, while the Monte Carlo Glauber model, the theory behind the T<sub>R</sub>ENTo-implementation, as well as a description of the code itself are discussed in **Chapter 4**. **Chapter 5** and **6** are dedicated to the hydrodynamical model and the model-to-data study on the impact of different parametrizations used to calculate initial conditions in T<sub>R</sub>ENTo. In **Chapter 7** the results of this thesis are summarized and an outlook on further studies on initial conditions are given.

# Chapter 2

## Heavy-Ion-Physics and the QGP

In this chapter the general physics background behind relativistic heavy-ion collisions is established and a new state of matter, the quark-gluon plasma (QGP), is introduced.

### 2.1 Standard Model, Quarks and QCD

The underlying theory in particle physics that is used to classify all particles (already discovered) and fundamental interactions (except for gravity), is the **Standard Model** of particle physics (SM). Within the standard model, all elementary particles can be grouped into three categories: quarks, leptons and gauge bosons. Additionally, respective antiparticles exist for quarks and leptons. Both carry half-integer spins and are therefore fermions. Leptons and quarks are further grouped into three generations [4]. Fig. 2.1 illustrates the classifications of particles and gauge bosons within the SM.

In this thesis we mainly focus on the study of strongly interacting matter under extreme conditions, which is why we will only focus on particles that interact via the strong interaction, namely quarks and gluons, also referred to as partons.

#### Quarks, Gluons and QCD

In contrast to leptons, which interact only via the weak and electromagnetic interaction, quarks can additionally interact via the strong interaction. Analogous to the electric charge for the electromagnetic interaction, only particles that carry a non-zero color charge can interact via the strong interaction. There are three different types of color charge states (plus three anti-colors): red (anti-red), blue (anti-blue), green (anti-green). The strong interaction, which is the predominant force only for short ranges ( $\sim 1$  fm), is mediated by eight massless gluons, that also carry color charges.

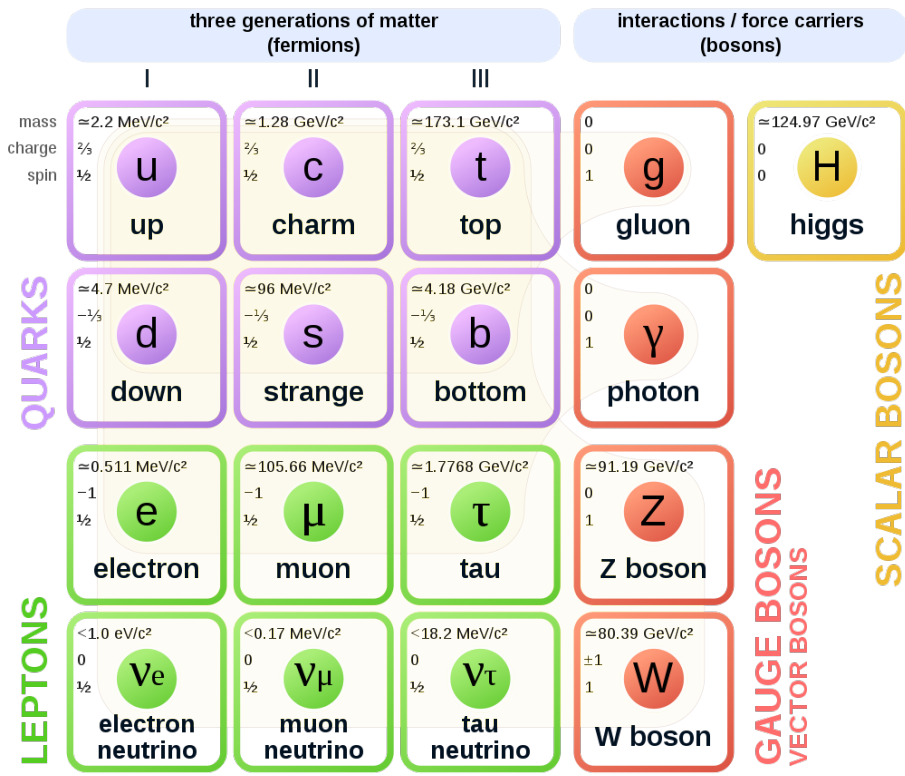


Figure 2.1: The fundamental structure of the Standard Model of particle physics. The fundamental particles and Gauge bosons are represented as building blocks and grouped into categories. The fermions are furthermore sorted into the three generations of matter, shown in ascending order from left to right. (Figure adapted from [3].)

Since particles that carry a non-zero color charge can couple to gluons and gluons themselves carry color charges, gluons can interact with other gluons.

The quantum field theory of the strong interaction is called **Quantum Chromo Dynamics (QCD)**. Two properties of QCD are **color-confinement** and **asymptotic freedom**, which are briefly explained in the following two sections.

### Color-Confinement

Although the existence of quarks has been confirmed by multiple experiments, free quarks have never been detected directly. One only detects quarks in color-neutral bound states of two quarks (mesons) as for example quark-anti-quark pairs ( $q\bar{q}$ ) or quark-triplets (baryons), like e.g. the proton. States of bound quarks are collec-

tively called hadrons. The fact that quarks usually exist in bound hadronic states is explained by 'color-confinement', meaning that particles with non-zero color charge cannot propagate freely. A qualitative explanation for color-confinement can be given when looking at the potential and the force between two color-charged object, e.g. a quark ( $q$ ) and an anti-quark ( $\bar{q}$ ). The non-relativistic QCD-potential for the bound  $q\bar{q}$ -pair has the following form [5]:

$$V(r) = -\frac{4}{3} \frac{\alpha_s}{r} + kr \quad (2.1)$$

Here  $r$  is the distance between the two quarks,  $\alpha_s$  denotes the strong coupling constant, and  $k$  is a constant with a value of  $\sim 1 \text{ GeV fm}^{-1}$ . The second term of the potential is proportional to the separation of the quarks  $r$  (for scales above the dimensions of a nucleus). Due to gluon-gluon coupling, the field-lines between the quarks are confined into 'tubes'. Equation 2.1 implies that the energy to separate the quarks infinitely, is infinitely high and therefore they are confined by the color-potential. That means that if  $q$  and  $\bar{q}$  are separated far enough, the energy to keep the pair separated is so large that it is energetically more convenient to create a second  $q\bar{q}$ .

### Asymptotic freedom

The strong coupling constant  $\alpha_s$  indicates how strong the coupling between the gluons and the corresponding color charge carrying particle is. It strongly depends on the energy scale  $Q$  of the interaction. In Fig. 2.2 the coupling constant as a function of  $Q$  in GeV is plotted;  $Q^2$  denotes the 4-momentum transfer of the respective interaction. The data points show measurements of the strong coupling constant at different energy scales. As indicated by the shape of the curve,  $\alpha_s$  decreases with increasing energy scales (or respectively larger momentum transfers). Consequently, the coupling between quarks decrease for large energy transfer until they behave as asymptotically free particles. This property of the strong coupling constant is known as **asymptotic freedom**.

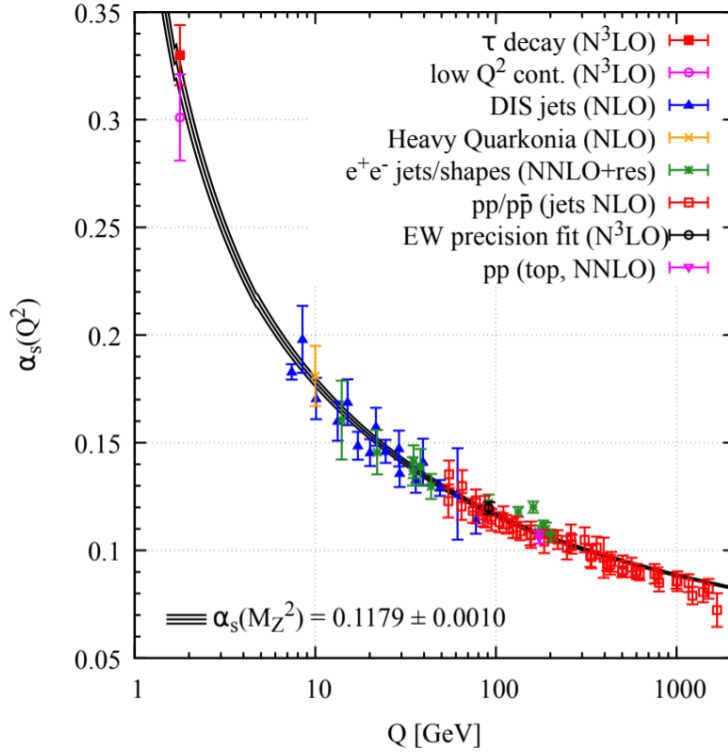


Figure 2.2: Running coupling constant of QCD as a function of the energy scale  $Q$  of the interactions. (Figure adapted from [6].)

## 2.2 QGP in Heavy-Ion Collisions

A few microseconds after the Big Bang the universe was filled with hot and dense matter consisting of only weakly bound strongly-interacting quarks and gluons. This type of matter is called **quark-gluon plasma** (QGP) [7]. Nowadays, such matter can be recreated during the collisions of heavy ions at large collider facilities such as the **L**arge **H**adron **C**ollider (LHC) near Geneva or the **R**elativistic **H**eavy **I**on **C**ollider (RHIC) on Long Island in the US. The running coupling constant in QCD indicates that at sufficiently high temperatures and/or large energies a phase transition between hadronic and deconfined quark-gluon matter should exist. The idea behind that is rather simple. Hadrons have a finite size of approximately 1 fm. If one considers a gas of hadrons at energy densities above 1 GeV per hadron, the hadrons overlap. This means that their constituents, quarks and anti-quarks as well as gluons, are located so close to each other that they cannot be assigned to one specific hadron anymore. They form a type of matter analogous to the plasma in **Q**uantum **E**lectro **D**ynamics (QED) [8].

The existence of the QGP was first suggested by the theoretical physicists J.C. Collins and M. J. Perry in 1975 [9]. In order to test these hypotheses experimentally, for example the Relativistic Heavy Ion Collider (RHIC) at the Brookhaven National Laboratory in the US was built in the mid 90's. At RHIC gold ions were collided with an energy of 200 GeV per nucleon pair. At the time of RHIC's construction, measurements of fixed target collisions, in which protons were collided with resting heavy-ion targets, had already been performed at e. g. the **A**lternating **G**radient **S**ynchrotron (AGS) in Brookhaven and at the **S**uper **P**roton **S**ynchrotron (SPS) at CERN [10]. The results from these first experiments suggested the existence of strongly interacting but non-hadronic matter right after the collisions. Evidence for the existence of the QGP were strongly reinforced by measurements at RHIC [11, 12]. Since 2010 the Large Hadron Collider (LHC) at CERN started to take data from various heavy-ion collisions of different systems including lead-lead (Pb-Pb) and xenon-xenon (Xe-Xe). The study of oxygen-oxygen (O-O) is planned for a future run.

### 2.2.1 Evolution in Space-Time

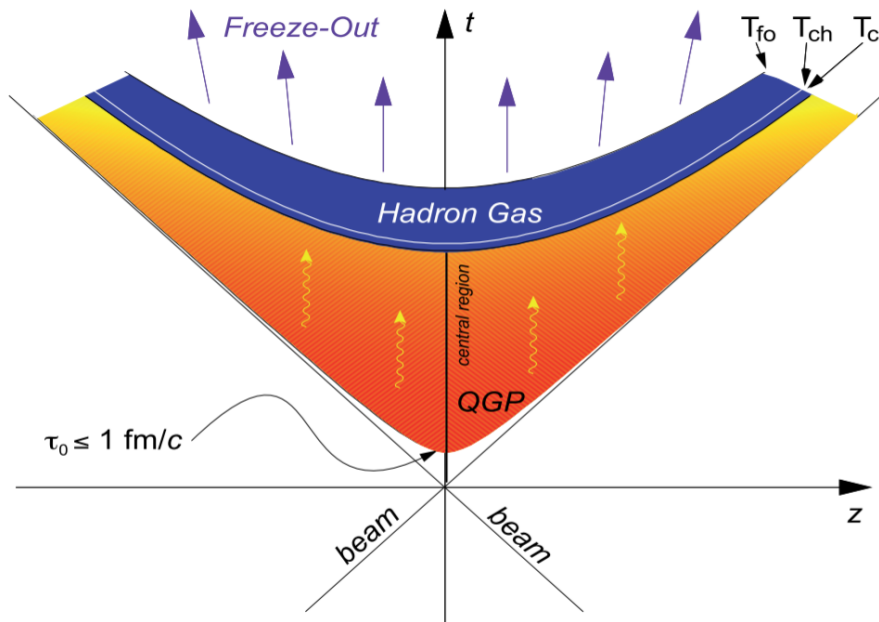


Figure 2.3: Different stages of the QGP evolution in space-time. (Figure adapted from [13].)

Prior to their collision, the nuclei are accelerated until their speed is almost equal to the speed of light. Hence, the nuclei are Lorentz contracted in the longitudinal

beam direction. To illustrate the impact of that contraction, we consider the dimensions of a lead nucleus. The diameter of a lead nucleus is approximately 14 fm. Due to the Lorentz contraction, the thickness of the nucleus is  $\frac{14}{\gamma}$ . Consequently, at the LHC at  $\sqrt{s_{NN}} = 2.76$  TeV and  $\gamma=1400$ , the thickness of the nucleus is only 0.01 fm [14].

The evolution of the QGP, created during heavy-ion collisions, can be separated into different stages. During the collision of the relativistic nuclei, tens of thousands of partons are created. Consequently, entropy and energy density are so high that the partons do not interact as individual particles but as a collective medium. Thus one can describe certain stages of the evolution in terms of viscous hydrodynamics. The different stages of evolution are illustrated in a space-time diagram in Fig. 2.3 and explained in the following.

**1) Collision and pre-equilibrium stage:** At  $t=0$  and  $z=0$  the two nuclei discs collide (or overlap), quarks and gluons interact and a 'fireball' consisting of deconfined quarks and gluons is formed. At this point the system is not in equilibrium and therefore cannot be described by fluid dynamics. Due to frequent collisions of the constituents, the system quickly thermalizes, meaning that a 'local' equilibrium is established. The duration of this pre-equilibrium stage is characterized by the thermalization time  $\tau_0$ , which is between  $0.1-1$  fm  $c^{-1}$ .

**2) Hydrodynamic evolution:** After the time  $\tau_0$  the matter is in local thermal equilibrium and can be described by relativistic fluid dynamics. Only at this stage the matter is referred to as quark-gluon plasma. The internal thermal pressure of the matter acts against the surrounding vacuum, causing the QGP to expand and cool down rapidly. The energy density of the system decreases.

**3) Hadronization:** Below a critical energy density of  $\epsilon_{crit} \leq 1$  GeV  $\text{fm}^{-3}$  and a critical temperature  $T_C$  a 'cross-over' between the deconfined QGP state and a confined state with hadronic degrees of freedom occurs. In conjecture to the occurring phase transition, the QGP reconfines into a hadron gas. The hadron gas is still in local thermal equilibrium due to collisions (inelastic and elastic) between its constituents. The system continues to expand and cools down.

**4) Freeze-out:** At the **chemical freeze-out temperature**  $T_{ch}$ , the number of inelastic collisions between the constituent hadrons becomes too small to keep up with the expansion rate. The hadrons cannot change their species anymore and the hadron abundances stay fixed. Nevertheless, elastic collisions maintain the local-equilibrium. Expansion and cooling of the system continue until the temperature of the system reaches the **kinetic freeze-out temperature**  $T_{kin}$ . If the system is cooler than that, the average mean-free path between the hadrons becomes larger than the range of the strong-interaction. This results in less frequent collisions that lead to a breakdown of the thermal equilibrium and the validity of the hydrodynamical description. Afterwards, the momentum distribution of the hadrons is fixed [15].

### 2.2.2 Flow

The collective dynamics of particles produced during (ultra) relativistic heavy-ion collisions is quantified by the observed particle anisotropies, that are expressed in terms of flow coefficients. In more general terms this phenomenon is called *collective flow*. As shown in Fig. 2.4, in non central collisions, the overlap region (colored in orange) of the colliding nuclei is generally not azimuthally symmetric (no angular symmetry in the x-y-plane). Due to the thermal pressure that builds up within the overlap region right after the collision, these spatial anisotropies are translated into anisotropies in momentum space over time, which leads to an azimuthal anisotropy in the particle production. The resulting anisotropy can be quantified by a Fourier decomposition of the azimuthal dependence of the experimentally measured, event-averaged particle spectra.

$$\frac{dN}{d\Phi} = \frac{N}{2\pi} \left[ 1 + 2 \sum_n v_n \cos[n(\Phi - \Psi)] \right] \quad \text{for } n = 1, 2, 3, \dots \quad (2.2)$$

Here  $\Phi$  denotes the azimuthal angle of the detected particle (in the transverse plane to the beam) and  $\Psi$  is the reaction plane angle. The reaction plane is depicted in Fig. 2.4, in this case the x-z-plane, but in general the plane perpendicular to the impact parameter  $b$ . The flow coefficients  $v_1$ ,  $v_2$  and  $v_3$  are called direct, elliptic and triangular flow. The existence of momentum anisotropies is denoted in non-zero anisotropic flow coefficients  $v_n$  for  $n \geq 2$  [16].

Originally, the QGP as it was postulated by theorists had been expected to be an ideal gas of weakly interacting partons that expands isotropically [9]. Initial measurements at RHIC showed a positive azimuthal anisotropy of the final particle spectra, quantified by elliptic flow measurements. Since calculations using hydrodynamics agreed with these results, it is shown that the QGP rather acts as an (ideal) fluid. From further measurements at RHIC and LHC as well as advances in Lattice QCD and viscous hydrodynamic calculations, nowadays, we know that the QGP acts as an almost perfect fluid with an extremely low shear viscosity over entropy ratio  $\eta/s$  [18]. The collective dynamics of the QGP are controlled by the shear viscosity over entropy ratio  $\eta/s$  and the bulk viscosity over entropy ratio  $\zeta/s$ .<sup>1</sup> In order to determine collective flow observables (such as the elliptical or triangular flow) at time  $\tau_0$  after the collision by calculating the hydrodynamic evolution, it is

---

<sup>1</sup>For readability, we will use  $\eta/s$  or  $\zeta/s$  instead of writing 'shear viscosity over entropy ratio' or 'bulk viscosity over entropy' in the remainder of the text.

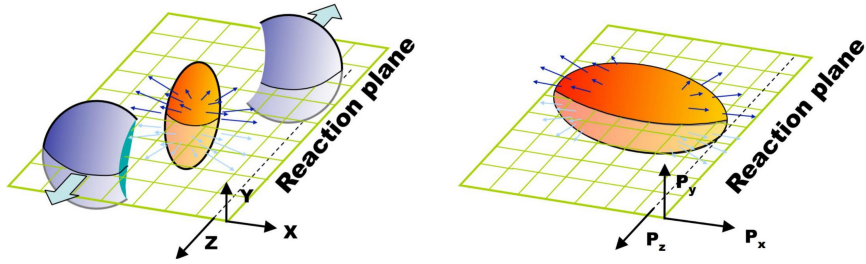


Figure 2.4: Non-central heavy-ion collision of two nuclei in position space (left) as well as in momentum space (right). On the left, the spatial asymmetry of the participant region (colored in orange) is shown. Due to thermal pressure against the vacuum, pressure gradients within the participant region build up. The spatial anisotropy causes the pressure gradient along the x-axis to be larger than along the y-axis. The resulting momentum anisotropy (referred to as *collective flow*) that builds up in the reaction plane is shown in the right picture. (Figure adapted from [17].)

essential to have an accurate initial condition model. This has to take into account fluctuations of the initial conditions [18, 16]. By fluctuating initial conditions one typically means the entropy or energy density profiles transverse to the beam. Due to fluctuations of the position of the nucleons inside the colliding nuclei as well as fluctuations of the energy density of individual nucleons themselves, these profiles are necessarily lumpy and asymmetric. Fluctuating initial conditions are especially important to explain the measurement of odd flow harmonics in head-on collisions. While non-fluctuating initial profiles for head-on collisions would imply that all odd  $v_n$ 's vanish, measurements at RHIC showed that in those collisions the triangular flow  $v_3$  is dominant [19].

# Chapter 3

## Kinematics in Relativistic Collisions

### 3.1 Collision Geometry

In this chapter, important concepts in order to describe and categorize collision events are introduced.

#### 3.1.1 Coordinate System

In order to analyze primary particles inside a detector as a result of a collision, it is essential to define a reference coordinate system. For such definition, we refer to the ALICE coordinate system [20]. The interaction point (IP) at the center of the detector is defined as the origin of the coordinate system while the z-axis is parallel to the mean beam direction. From now on, we will refer to the direction along the z-axis as longitudinal direction, while we denote the x-y-plane, which is perpendicular to the beam, as transverse plane. The reference coordinate system is illustrated in Fig. 3.1. The kinematics of a particle inside the detector is fully described by (the modulus of) its transverse momentum  $p_T = \sqrt{(p_x)^2 + (p_y)^2}$ , the azimuthal angle  $\phi$  and the polar angle  $\theta$ . Since  $\theta$  is not invariant under Lorentz boosts in the longitudinal directions, it is convenient to introduce the rapidity  $y$  which is defined as:

$$y = \frac{1}{2} \ln \frac{E + p_z c}{E - p_z c} \quad (3.1)$$

Here  $E$  denotes, the energy of the particle,  $p_z$  the momentum in the longitudinal direction and  $c$  the speed of light. The rapidity is additive under Lorentz boosts. At relativistic particle energies with  $E \approx pc \gg mc^2$ , the rapidity  $y$  is approximately

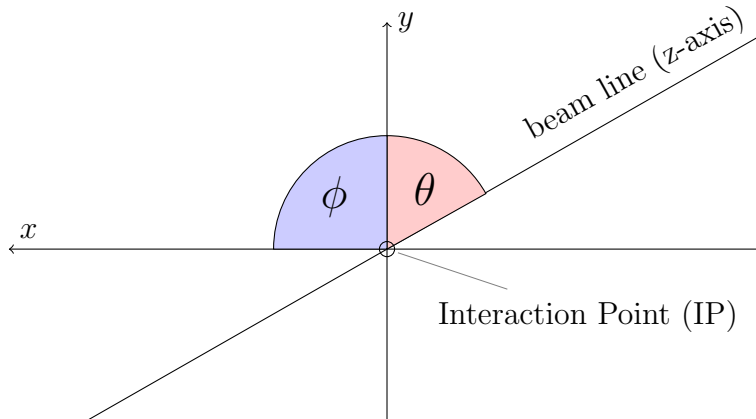


Figure 3.1: Reference coordinate system using the same notation that is used to describe the ALICE experiment. The polar angle in the y-z-plane is denoted as  $\theta$ . The angle in the transverse plane (x-y-plane) is denoted as  $\phi$ . (Figure inspired by [20].)

equal to the so-called pseudorapidity  $\eta$ ,

$$y \approx \eta = -\ln \tan \frac{\theta}{2} \quad , \quad (3.2)$$

which conveniently depends only on the polar angle  $\theta$ . (For reference of the introduced equations and concepts see [21].)

### 3.1.2 Experimental observables

The effects of the initial pre-equilibrium dynamics, the collective evolution and the freeze-out behaviour are captured by several experimental observables e.g flow coefficients or the  $p_T$ -integrated particle yield at mid-rapidity. In this thesis, we investigate the  $p_T$ -integrated particle yield per unit rapidity at mid-rapidity  $\frac{dN}{dy}$ , which is the (average) number (also called multiplicity) of charged particles per unit rapidity in the rapidity interval  $|y| < 0.5$ .  $\frac{dN}{dy}$  is proportional to the entropy density in the system [22] and therefore allows to draw conclusions about the pre-equilibrium phase of the QGP.

### 3.1.3 Event centrality

In heavy-ion collisions, the impact parameter  $b$ , defined as the distance between the center of masses of the colliding nuclei, cannot be measured experimentally. Only

the number of (charged) particles in the final state is detected. However, intuitively head-on collisions produce a larger final number of charged particles, (referred to as inclusive charged particle multiplicity  $N_{ch}$ ), compared to collisions with a larger impact parameter. Based on the underlying assumption that  $N_{ch}$  is related monotonically to the impact parameter and therefore the centrality of a collision, one defines *centrality classes* based on e.g. the final charged particle multiplicity distribution. In Fig. 3.2 an example for the assignment of centrality classes is illustrated. The 0-5% centrality class contains the 5% with the highest multiplicity of all detected events, the 5-10% class then corresponds to the next 5% and so on.

### 3.1.4 Main quantities

The colliding nuclei in a collision consist of nucleons (neutrons and protons). In terms of the Glauber model, described in detail in the next chapter, one distinguishes between nucleons that collide at least once (so called *participants*) and nucleons that don't collide at all (so called *spectators*). The number of participants (and spectators) is denoted as  $N_{part}$  (and  $N_{spec}$ ). The total number of nucleon-nucleon collisions is called the number of binary collisions  $N_{coll}$ .

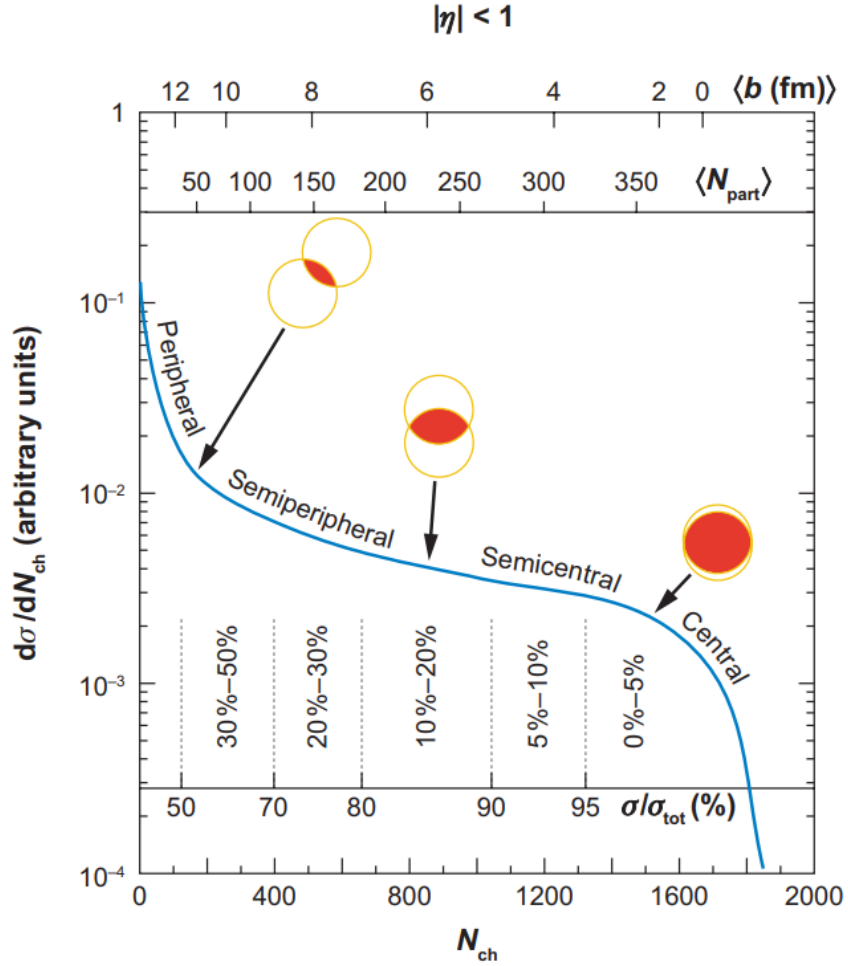


Figure 3.2: The slicing of a multiplicity distribution (blue line) in terms of event centrality is illustrated. Furthermore, the overlap area of the colliding nuclei for different centralities is sketched schematically in red. The most central events at small impact parameter  $b$  produce the largest multiplicity values, while more peripheral events with a larger impact parameter produce lower multiplicities. (Figure adapted from [23].)

# Chapter 4

## Initial State description

In this chapter, we introduce the initial condition model T<sub>R</sub>ENTo that is based on the Monte Carlo Glauber model. The T<sub>R</sub>ENTo model is able to simulate initial conditions for a hydrodynamic description of the QGP produced in ultra-relativistic heavy-ion collision. We briefly explain the main assumptions and characteristics of the Glauber model and finally discuss the initial condition model T<sub>R</sub>ENTo that uses a Monte Carlo Glauber approach to calculate the initial transverse entropy (or alternatively energy) density profiles of the collision at the time of the QGP's thermalization  $\tau_0$ .

### 4.1 About Initial Conditions

As already mentioned in **Chapter 1**, it is possible to describe certain stages of the QGP evolution in terms of viscous hydrodynamics. Since the system undergoes a pre-equilibrium evolution between the collision and the moment where it is described in terms of viscous hydrodynamics, phenomenological initial condition models are used, since their direct experimental determination is not possible. For any hydrodynamic simulation of high energy collisions it is necessary to provide information on the macroscopic quantities of the quark-gluon fluid that forms. Such quantities are typically, the temperature (calculated from initial entropy profiles via an equation of state) as well as velocity fields and transport coefficients [24]. While various initial condition models with different physical motivations exist, we only introduce the Glauber model which is relevant for the work presented here.

### 4.2 The Glauber model

One of the most successful theoretical descriptions of the collision of two nuclei at high energies is the Glauber Model. In the 1950s, the physicist Roy Glauber intro-

duced a quantum mechanical scattering theory for composite systems, which was later expanded and applied to inelastic nuclear collisions [25]. The remaining part from Glauber's original calculation was the 'optical limit approximation', which allows for numerical calculations of multiple scattering integrals. Nowadays, a Monte Carlo Glauber approach combined with an entropy production mechanism is commonly used to determine initial conditions, for ultra-relativistic collisions.

### 4.2.1 Background information

For a valid description of the QGP's initial state we need to understand the scattering process of two nuclei at high energies. Roy Glauber introduced a theory that describes the collision at high energies of the two nuclei as a superposition of collisions of their corresponding nucleons. Models that rely on this concept are generally referred to as *Glauber models*.

Glauber calculations themselves depend on the input of two quantities: the nuclear density distribution (obtained from low energy scattering experiments), which provides a geometrical description of the colliding nuclei as well as the energy dependence of the inelastic nucleon-nucleon cross section.

In the next section, we briefly introduce the basic concept of the Glauber calculations based on the 'Optical limit approximation' used to calculate macroscopic quantities such as  $N_{part}$ ,  $N_{coll}$  and the cross section of the nuclei collision analytically. Optical limit Glauber calculations and the Monte Carlo Glauber ansatz both rely on the assumption that in case of the nucleus-nucleus collision, the constituent nucleons travel on straight trajectories and are not deflected when the nuclei pass through each other. This assumption is justified since the colliding nuclei carry a sufficiently large momentum in ultra relativistic collisions.

### 4.2.2 Analytical calculations within the Glauber Model

Under the "optical limit approximation" one can draw the following schematic picture (Fig. 4.1) of a nucleus-nucleus collision in transverse and longitudinal views. The distinction between target and projectile is only made for convenience and does not imply that the picture is only valid for fixed target collisions.

In this section we follow the notation that is introduced in [23]. We consider the collision of nuclei A and B containing A and B nucleons, respectively. For an analytic calculation of Glauber quantities ( $N_{part}$ ,  $N_{coll}$  or the total cross-section for an interaction between nuclei A and B), we introduce the *thickness function*  $T_{AB}$ . The function quantifies the effective overlap area between the target and the projectile in the transverse plane in which nucleons from both nuclei can interact. It is defined

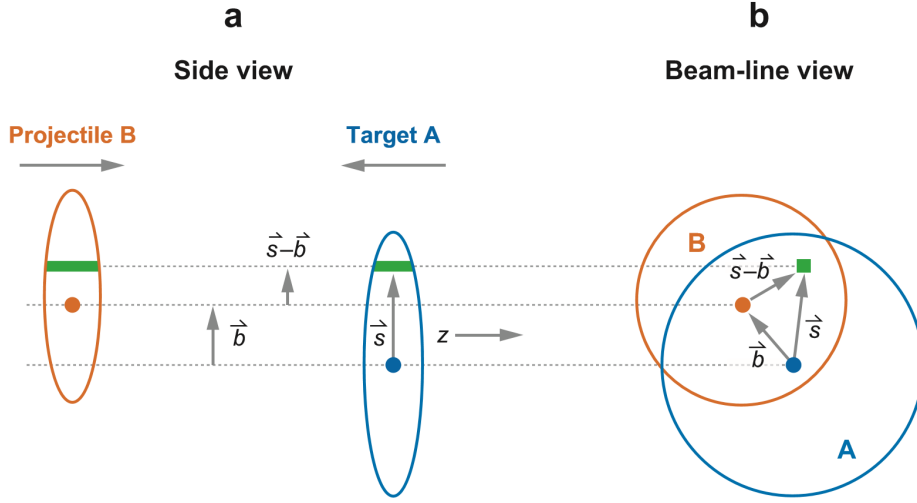


Figure 4.1: Representation of the collision of two nuclei as described by the optical Glauber Model; transverse (a) and longitudinal (b) view. The distinction between projectile (orange) and target (blue) is only made for convenience. Figure adapted from [23].

as:

$$T_{AB} = \int T_A(\vec{s}) T_B(\vec{s} - \vec{b}) ds^2 \quad . \quad (4.1)$$

where

$$T_A = \int \rho_A(\vec{s}, z_A) dz_A \quad (4.2)$$

( $T_B$  analogous). Here,  $\rho_{A(B)}(\vec{s})$  denotes the nuclear density, meaning the probability per unit volume of finding a nucleon at the position  $\vec{s} = (x, y, z)$  inside the nucleus. This probability distribution is typically parameterized by a Wood-Saxon distribution [26]. Since  $T_A$  gives this probability distribution integrated in  $z$ -direction, it defines the nuclear density projected onto the transverse plane. The probability  $P_{coll}$  for an interaction between two nucleons is then given by

$$P_{coll} = T_{AB} * \sigma_{inel}^{NN} \quad (4.3)$$

where  $\sigma_{inel}^{NN}$  denotes the inelastic cross section for nucleon-nucleon collisions. Since elastic collisions between the nucleons do not play an important role at the energies considered here, they are neglected for Glauber calculations.

With those expressions at hand it is possible to write down analytic expressions for the number of participants, the number of binary collisions or the total inelastic cross-section for the collision of the two nuclei as a function of the impact parameter  $b$  (see [23]).

### 4.2.3 Monte Carlo Glauber Approach

In the Monte Carlo Glauber ansatz, Glauber quantities are determined slightly differently. First, for each simulated event, the nucleons are assembled in a 3D coordinate system according to the 3D nuclear density distribution of the respective nuclei. Secondly, a random impact parameter is sampled from the following distribution:

$$\frac{d\sigma}{db} = 2\pi b \quad (4.4)$$

If the distance between two nucleons is small enough, one considers the nucleons to collide. An iteration over a large number of events then leads to event averaged values of  $N_{part}$ ,  $N_{coll}$  and also the charged particle multiplicity per unit rapidity  $\frac{dN}{d\eta}$ . Since the latter is an experimentally measurable observable, it can be directly related to measurements.

In contrast to analytical optical limit Glauber calculations, the Monte Carlo Glauber ansatz assumes a discrete position of each nucleon within the nucleus instead of assuming a continuous nuclear density distribution. This has a measurable effect on the total cross section of the A+B collision (for reference see [23], section 2.5).

## 4.3 Trento

The non-dynamical initial condition model **T<sub>R</sub>ENTo** (**R**educed **T**hickness **E**vent-by-event **N**uclear **T**opology) was designed to produce transverse entropy density profiles at the QGP's thermalization time using a Monte Carlo Glauber approach and the introduction of a reduced thickness function that is proportional to the entropy deposited in the transverse plane at mid-rapidity.

The idea behind it is simple: Each nucleon-nucleon collision is assumed to deposit a 'blob' of entropy at the position of the collision in the plane transverse to the beam during the collision. In case of the collision of two nuclei, the entropy profile is composed of the entropy 'blob' of each nucleon-nucleon collision. **T<sub>R</sub>ENTo** itself is a Monte-Carlo simulation that calculates the profile for each event individually. [27] A routine to average output quantities from **T<sub>R</sub>ENTo** over several events has to be implemented separately.

### 4.3.1 Algorithm

The ansatz used in **T<sub>R</sub>ENTo** is heavily inspired by a two component Monte Carlo Glauber ansatz. The approach that is presented in [27] is very similar to the one

described in **Section 4.2.3**. For references of equations and concepts we refer to [27].

Let us now have a look at the approach used for simulating the collision of two projectiles A and B (they may be protons or two nuclei of the same or of different elements) in T<sub>R</sub>ENTo. The position of the nucleons is sampled from a Wood-Saxon's distribution of the following form:

$$\rho(r) = \frac{\rho_0}{1 + \exp[(r - R)/a]} \quad (4.5)$$

where  $\rho_0$  is the nuclear density at the center of the nucleus,  $R$  the nuclear radius,  $a$  is the skin depth.

Secondly, the collision probability is sampled for each pairwise interaction to determine the number of participants in the collision. The collision probability of two nucleons is:

$$P_{coll} = 1 - \exp \left[ -\sigma_{gg} \int dx dy \int dz \rho_A \int dz \rho_B \right] \quad (4.6)$$

Here,  $\sigma_{gg}$  denotes the effective parton-parton cross section such that the total proton-proton cross section is equal to the experimentally used inelastic nucleon-nucleon cross section. As a next step, the nucleon density distribution integrated over  $z$  of each colliding nucleon (equal to Eq. 4.2 but in this case for nucleons instead of nuclei) is then weighted by a gamma weight factor  $w_i$  (for each participant  $i$ ), which is randomly sampled from a gamma distribution of the following form:

$$P_k(w) = \frac{k^k}{\Gamma(k)} w^{k-1} e^{-kw} \quad (4.7)$$

This *fluctuated thickness function* of each colliding nucleon then takes the following form:

$$T_{i,f} = w_i \int dz \rho_i(x, y, z) \quad (4.8)$$

for  $i=A,B$ .

The reason for implementing weights to induce a fluctuation of the thickness function is, that the number of partons produced in a nucleon-nucleon collision fluctuates event-by-event. Hence, the entropy deposited by each nucleon-nucleon collision fluctuates event-by-event [28].

The parameter  $k$  determines how large these fluctuations are. For  $0 < k < 1$ , the fluctuations are enhanced, for  $k \gg 1$  they are suppressed within the model. The *fluctuated thickness function* for the nuclei A and B in the end has the following form:

$$T_{A(B),f} = \sum_{i=0}^{N_{part}} w_i \int dz \rho_{proton}(x - x_i, y - y_i, z - z_i) \quad (4.9)$$

Finally, the T<sub>R</sub>ENTo model introduces a reduced thickness function  $T_R$  which is proportional to the entropy in the system at mid-rapidity at times of the thermalization of the QGP, so  $\frac{dS}{dy}|_{\tau=\tau_0}$ .

The *reduced thickness function* is defined as the generalized mean of the (fluctuated) thickness functions  $T_{A,f}$  and  $T_{B,f}$ :

$$T_R = \left( \frac{T_{A,f}^p + T_{B,f}^p}{2} \right)^{1/p} \quad (4.10)$$

The  $p$ -values determines how the mean of the participant thicknesses is taken that at the end, corresponding to the amount and the place of the entropy deposited in the system. For  $p = 0$  for example, the reduced thickness function corresponds to the geometric mean of the (fluctuated) participant thicknesses. In Fig. 4.2, the reduced thickness function for three different  $p$ -values is shown. As one can see, going from  $p = -1$  to larger values of  $p$  the cross section of the reduced thickness function broadens. At this point it is important to notice that  $p$  is not a discrete but continuous variable.

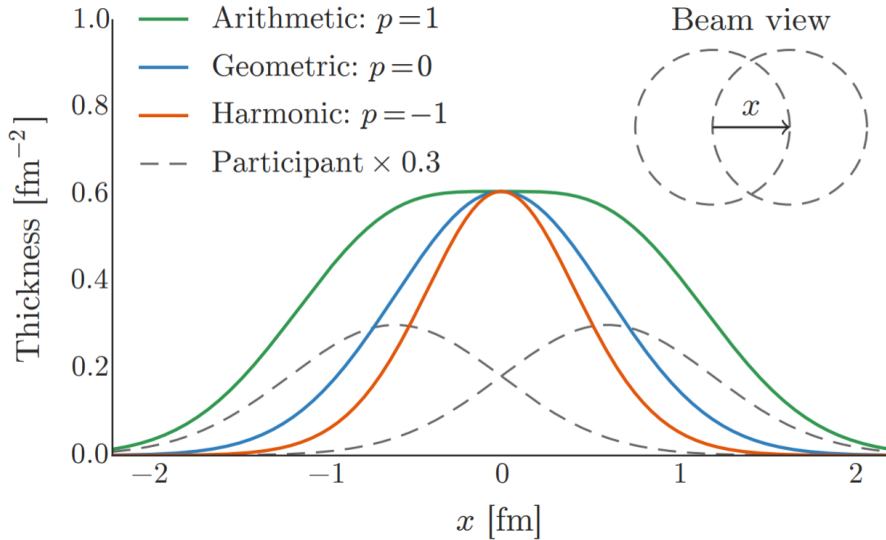


Figure 4.2: Reduced thickness function for the collision of two protons (without fluctuations). For the nucleon participant thickness function a two dimensional Gaussian profile was assumed (as implemented in T<sub>R</sub>ENTo). The figure shows a cross section ( $y=0$ ) of the participants (grey dashed lines) and reduced thicknesses (colored lines). Figure adapted from [27].

The optimal values for  $k$  and  $p$  have to be determined for each collision system individually by a systematic model to data comparison. For the upcoming analysis, we followed the values that are presented in [27], but chose to widen the range of  $p$ .

### 4.3.2 Brief description of the code

The T<sub>R</sub>ENTo code is openly accessible on github [29]. A documentation of the its usage can be found in [30].

#### Input

There are several options that can be specified before running the code, that influence the physical behavior of the T<sub>R</sub>ENTo model. First of all the projectiles, as well as the number of events, have to be specified. Furthermore the inelastic nucleon-nucleon cross section, the  $p$ - and  $k$ -parameter (see Eq. 4.10 and 4.7) have to be specified. For the nuclear thickness function of the constituent nucleons, the model assumes a two dimensional Gaussian shape. The corresponding Gaussian nucleon width  $w$  can be specified before running. Since the reduced thickness function of the projectiles is calculated on a two dimensional  $N \times N$ -grid, the grid proportions have to be specified as well. The entire list of optional input parameters can be found in the documentation [30].

#### Output

For each event that is simulated in T<sub>R</sub>ENTo, the code produces a list of event-by-event properties as well as a two dimensional initial entropy density profile on a discretized grid, saved into a file. Examples are shown in Fig. 4.3. The event-by-event properties calculated by default are: The impact parameter  $b$ , the number of nucleon participants  $N_{part}$ , the (pseudo-)multiplicity (integrated reduced thickness function) as well as the eccentricity harmonics, which quantify initial spatial anisotropies of the participant region. If specified, the number of binary collisions  $N_{coll}$  can be calculated too.

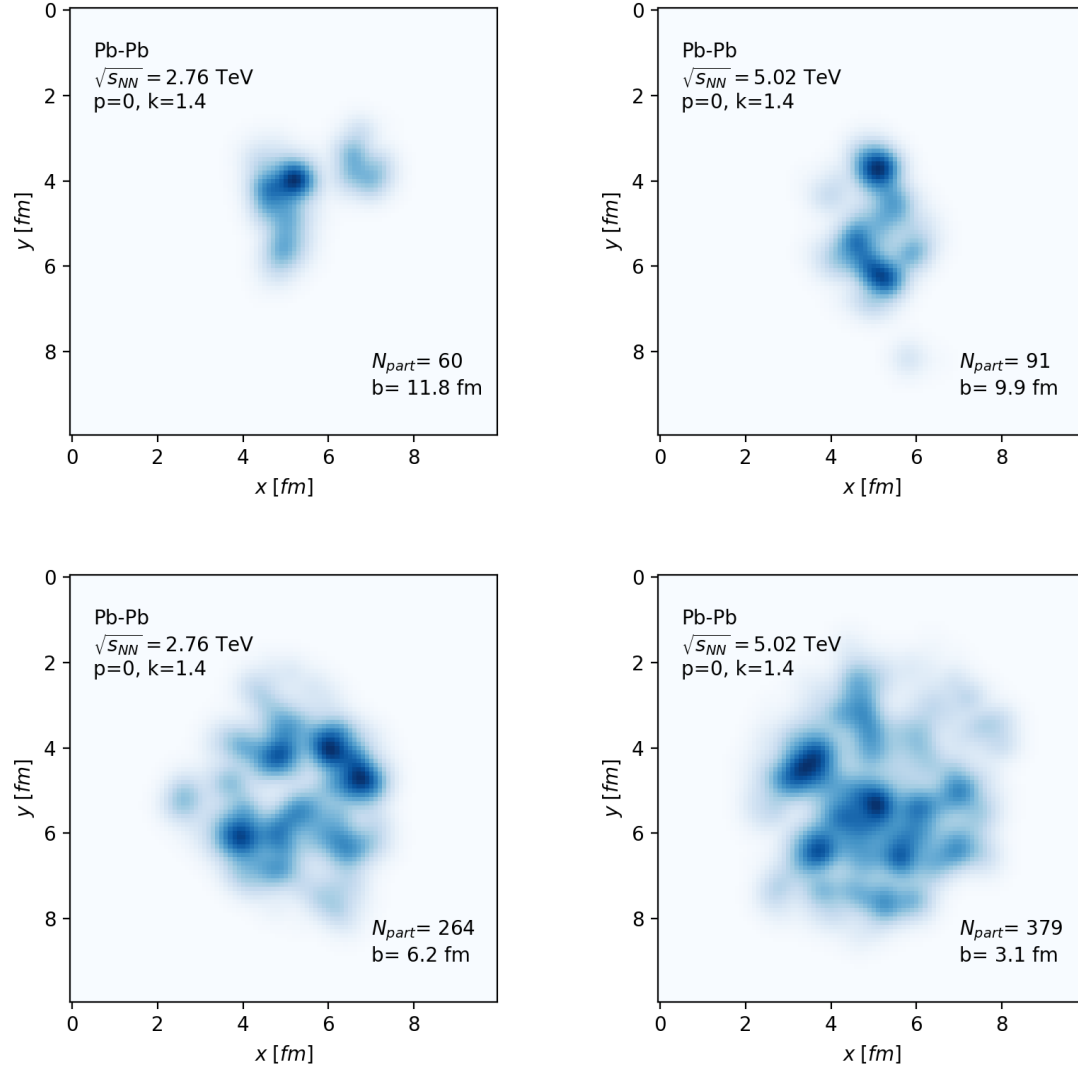


Figure 4.3: Various 'raw' entropy density profiles of Pb-Pb collisions at  $\sqrt{s_{NN}} = 2.76$  TeV and 5.02 TeV produced with T<sub>R</sub>ENTo. The impact parameter  $b$  and the number of participants  $N_{part}$  is specified for each example.

# Chapter 5

## Analysis Methods

### 5.1 Outline of the analysis

In the previous chapter we have outlined that an accurate initial state description is key to analyze the collective behavior of the QGP. Therefore, the Glauber Model and its application in the initial condition model T<sub>R</sub>ENTo were introduced. In [24] a systematic study was presented, comparing experimentally measured averaged transverse momentum spectra for pions, kaons and protons with theoretical calculations. With a global fit procedure, best fit parameters for  $\eta/s$ ,  $\zeta/s$ ,  $\tau_0$ ,  $T_{fo}$  and the *Norm* of the initial entropy density profile were determined. The theoretical set-up included three different parts: T<sub>R</sub>ENTo for initial conditions, the FluiduM package to solve the evolution equations of hydrodynamics and FastReso to take resonance decays that occur between freeze-out of the hadron gas and the final detection into account. This thesis aims to determine an optimal  $p$ -value for Pb-Pb at  $\sqrt{s_{NN}} = 2.76$  TeV and 5.02 TeV, using the same tools and the best fit parameters as in [24]. In this chapter, we discuss the methods and implementation for our analysis and verify our approach.

### 5.2 Initial conditions

#### 5.2.1 Implementation

To produce the initial conditions for FluiduM, a python program was written to determine the collision centrality based on average multiplicities from T<sub>R</sub>ENTo events. Furthermore, an already existing C++-program [31] was used to calculate the average entropy density profile in the transverse plane.

## Centrality determination

The centrality class determination we perform is based on the data of  $10^5$  collision events generated in T<sub>R</sub>ENTo. From that data, we want to determine the average multiplicities in 1%-centrality intervals, meaning that each interval contains one percentile of the integrated probability distribution. The procedure is illustrated in Fig. 5.1 and described in the following.

For each event, the multiplicity values from the T<sub>R</sub>ENTo output were read into numpy arrays in python. We generated a numpy.histogram and determined the probability density distribution, calling the class *scipy.stats.rv\_histogram* using the methods *pdf* for the probability distribution function and *cdf* for the cumulative distribution function. The probability distribution function and the cumulative distribution function are related in the following way:

$$cdf(\tilde{x}) = \int_0^{\tilde{x}} pdf(x) dx \quad (5.1)$$

Hereby *pdf*, is a step-wise function determined from the histogram, while *cdf* is an interpolation of *pdf*. For further details see the documentation [32]. First, the edges of the centrality intervals were determined. Therefore, the probability distribution function, *pdf*(*x*), was split into percentiles such that the following equation is satisfied for the edges of all intervals.

$$\int_{x_{low}}^{x_{up}} pdf(x) dx = 0.01 \quad (5.2)$$

Here  $x_{low}$  and  $x_{up}$  denote the lower and the upper edge of the interval. The average multiplicities are then calculated with the following equation:

$$\langle M (i \% - (i + 1) \%) \rangle = \frac{\int_{x_{low}}^{x_{up}} x pdf(x) dx}{\int_{x_{low}}^{x_{up}} pdf(x) dx} \quad (5.3)$$

for  $i \in (0, 99)$ .

## Averaged initial entropy density

In the following section we refer to the concepts and notations introduced in [2]. Let  $\epsilon(r, \Phi)$  be the entropy profile of a single event in the transverse plane, expressed in polar coordinates. The code we use to calculate the average transverse entropy density, aligns the 2D entropy density profiles such that the origin in the transverse plan is located at the center of mass of the colliding nuclei. For the calculation of the averaged initial entropy density, the following function is introduced:

$$W(r) = \frac{1}{2} \int_0^{2\pi} d\phi \langle \epsilon(r, \phi) \rangle \quad (5.4)$$

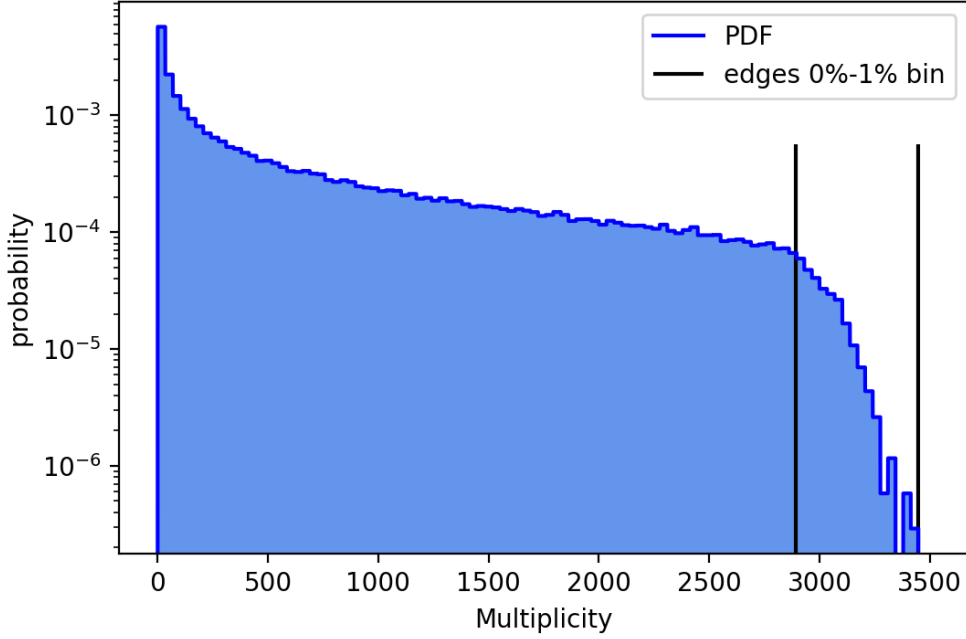


Figure 5.1: Illustration of the centrality slicing into 1% centrality intervals. The dark blue line illustrates the probability density function of the numpy.histogram of (pseudo-) multiplicity from T<sub>R</sub>ENTo. The two vertical black lines indicate the multiplicity values that denote the edges of the 0-1% centrality intervals. For more details see the text.

Here  $\langle \epsilon(r, \Phi) \rangle$  denotes the entropy profiles averaged over an ensemble of events of the same centrality class.

The entropy profiles are normalized such that the following condition is fulfilled for all events:

$$\int_0^\infty dr r \int_0^{2\pi} d\phi \epsilon(r, \phi) = 1 \quad (5.5)$$

The program [31], that was used calculates the values of  $W(r)$  for a number of discrete radii for each of the previously defined 100 centrality intervals, is based on the output of  $10^5$  events sampled with T<sub>R</sub>ENTo.

### 5.3 Hydrodynamic evolution and Resonance decays

Since we discussed the initial condition model T<sub>R</sub>ENTo and its implementation in detail, what is left to do is to introduce the missing two components of the theoretical model. The FluiduM package code is used to describe the evolution of the QGP in terms of viscous relativistic fluid dynamics. To account for the strong and electromagnetic decays of short-lived hadrons after the freeze-out of the QGP but before the particles are detected, the publicly available code FastReso is used (to calculate so called decay-kernels). In this section we follow the concepts and notations introduced in [2, 24].

#### Overview on FluiduM and FastReso

In our set-up, the FluiduM package code is used to solve the hydrodynamic equations of motion. These are non-linear, hyperbolic differential equations, which require certain initial conditions that are obtained from T<sub>R</sub>ENTo using the implementations described in the previous section. The time between the collision and the start of the hydrodynamic evolution is then specified by the thermalization time  $\tau_0$ , which is a free parameter in FluiduM. From the initial conditions, the averaged entropy density profile for each centrality class in the transverse plane is calculated in FluiduM as

$$s(r) = \frac{Norm_i}{\tau_0} \langle T_R(r, \phi) \rangle \quad . \quad (5.6)$$

$\langle T_R(r, \phi) \rangle$  denotes the averaged reduced thickness function calculated in T<sub>R</sub>ENTo that was introduced in the previous chapter. If an ideal initial condition model is used, we assume that the normalization constant  $Norm_i$  is the same for all centrality classes. Contrary to that, the result obtained in [24] indicated that the normalization constant is somewhat centrality dependent. In general, the FluiduM package approaches relativistic viscous fluid dynamics working with mode expansions. The fluid field is split into a background and a fluctuation (or perturbation) part as  $\Phi(\tau, r, \phi, \nu) = \Phi_0(\tau, r) + \Phi_1(\tau, r, \phi, \nu)$ . Here  $\Phi_0$  is the background field which is symmetric under azimuthal rotations and boosts along the longitudinal direction. The fluctuation field  $\Phi_1$  does not exhibit these symmetries. It can be subject to event-by-event fluctuations, which arise from either statistical or quantum fluctuations. Hence an expansion scheme is applied to the fluctuation fields which allows to expand the transverse entropy density ( $W(r)$ ) in terms of Bessel functions. Background and fluctuation field can then be evolved separately. The evolution incorporates bulk and shear viscous corrections. The equation of state in FluiduM is based on Lattice QCD calculations and given in [2]. At the temperature  $T_{fo}$  the FluiduM code converts

the fluid fields into particle distributions according to a Cooper Fry procedure (see [33] for reference). Therefore, the spectrum of hadron species (denoted by  $a$ ) on the freeze-out hypersurface  $\Sigma$  is given by

$$E_p \frac{dN_a}{d^3p} = \frac{\nu_a}{(2\pi)^3} \int_{\Sigma} f_a(\tilde{E}_p) p^\mu d\Sigma_\mu \quad . \quad (5.7)$$

Here,  $\nu_a$  denotes the degeneracy factor of the spin/polarization states and  $f_a(\tilde{E}_p)$  the particle distribution function at the fluid rest-frame  $\tilde{E}_p = -u^\nu p_\nu$  where  $u^\nu$  is the covariant 4-velocity and  $p_\nu$  the 4-momentum of the fluid. The particle distribution function is then given by an equilibrium Bose-Einstein or Fermi-Dirac distribution (depending on the spin of the species) modified by correction terms accounting for bulk and shear viscous dissipation.

$$f = f_{eq} + \delta f^{bulk} + \delta f^{shear} \quad (5.8)$$

To finally calculate the invariant yields  $\frac{dN}{2\pi p_T dp_T dy}$ <sup>1</sup> for different particle species, a calculation of decay kernel (that takes into account the decay of unstable resonances) with the code FastReso is necessary. The resulting spectra can be compared to experimentally measured  $p_T$ -spectra of identified hadrons. For more details on the implementations in FluiduM and their theoretical motivation we refer to [2] and the references therein.

### Physical assumptions of our implementation

Along the lines of the FluiduM set-up that was used for the work presented in [24], we are only interested in evolving the background field. As our goal will be to quantify the impact of varying initials conditions on the averaged transverse  $p_T$ -integrated spectra, this constraint is justified since the averaging takes care of the fluctuation part. In this thesis we also make the same physical assumptions as in [24]. Therefore, we assume  $\eta/s$  to be independent of temperature and  $\zeta/s$  to be temperature dependent.  $\zeta/s$  is assumed to have a Lorentzian form:

$$\zeta/s = \frac{(\zeta/s)_{max}}{1 + \left(\frac{T-175 \text{ MeV}}{24 \text{ MeV}}\right)^2} \quad (5.9)$$

The equation was taken from [24].  $(\zeta/s)_{max}$  is the input parameter to FluiduM. Furthermore, the FluiduM implementation does not distinguish between kinetic and

---

<sup>1</sup>also referred to as particle spectra

chemical freeze-out. This means that at chemical freeze-out, FluiduM assumes that the fluid elements, (that characterize the hadron gas) are converted into thermal particles. Those that are unstable resonances are then immediately converted into their decay products and do not rescatter with one another. Subsequently, kinetic and chemical freeze-out are assumed to happen at the same temperature, which is denoted with  $T_{fo}$ .

### Technical implementation in Mathematica

The FluiduM code package is written in Mathematica in terms of separate functions that can be called to perform various steps of the hydrodynamic evolution. Pre-calculated decay-kernels are also part of the FluiduM-code package. Prior to a calculation, several input parameters have to be specified. For this set-up these are:  $\eta/s$ ,  $\zeta/s$ ,  $\tau_0$ ,  $T_{fo}$ ,  $Norm_i$  and the initial conditions. Additionally, a grid that is used to solve the partial differential equations of motion, as well as the  $p_T$ -range for the final spectra calculation has to be initialized. Furthermore, an additional option to choose from different initial condition files featuring T<sub>R</sub>ENTo initial conditions calculated with different p-values had been implemented. For our purposes, we set up a routine in Mathematica including the following steps:

- Parametrizing a QCD viscous fluid with transport coefficients  $\eta/s$  and  $\zeta/s$ ;
- Setting up the initial conditions;
- Solving the equation of motion for the background fields;
- Interpolating the previous solution in space and time to determine thermodynamic quantities on the freeze-out surface;
- Calculating the Lorentz covariant particle spectra (including resonance decays) and extracting the multiplicity.

## 5.4 Verification of the setup

To validate our final result in the end, it is necessary to first verify the (combined) setup of T<sub>R</sub>ENTo and FluiduM, by a comparison to previous work with FluiduM. In [24] a global fitting procedure is presented to determine the best model parameters for FluiduM, based on the comparison to experimentally determined averaged transverse  $p_T$ -spectra in Pb-Pb collisions at energies of  $\sqrt{s_{NN}} = 2.76$  TeV measured in ALICE

at the LHC.

The first step was to check that our set-up could reproduce the  $p_T$ -integrated yields at mid-rapidities ( $|y| < 0.5$ ) with our set of initial conditions. Therefore, two major checks were done. First a direct comparison of the 'old' (as used in [24]) and the 'new' set of initial conditions; secondly via the FluiduM output for our set-up with new and old initial conditions.

For the direct comparison, we directly compared the values of the average multiplicity (see Eq. 5.3) calculated via a C++-routine ([31]) used for the work in [24] and via the method presented in **Section 5.2** based on an implementation in python. For a simulation of  $10^5$  Monte Carlo events in T<sub>R</sub>ENTo, the parameters in **Table 5.1** were used. We denote the result from the C++ code as  $\langle M \rangle_{old}$  and the results from

projectiles	Pb-Pb	Norm <sub>1</sub> (0-5% cent)	54.2
number of events	$10^5$	Norm <sub>2</sub> (5-10% cent)	55.3
reduced thickness ( $p$ )	0	Norm <sub>3</sub> (10-20% cent)	56.1
fluctuation ( $k$ )	1.4	Norm <sub>4</sub> (20-30% cent)	56.9
nucleon-width $w$	0.6 fm	Norm <sub>5</sub> (30-40% cent)	56.9
NN cross-section ( $\sigma_{NN}^{inel}$ )	$6.4 \text{ fm}^2$	$\tau_0$ [fm c <sup>-1</sup> ]	0.179
normalization	1	$\eta/s$	0.164
grid-max	10 fm	$(\zeta/s)_{max}$	0.059
grid-step	0.2 fm	$T_{fo}$ [MeV]	137.1

Table 5.1: T<sub>R</sub>ENTo- and FluiduM model parameter. Both are used for the comparison of the two different methods to calculation of initial conditions presented in **Section 5.2** and with [31]. The best fit parameters for FluiduM are presented in [24].

our python implementation as  $\langle M \rangle_{new}$ . In Fig. 5.2, the ratio  $\frac{\langle M \rangle_{new}}{\langle M \rangle_{old}}$  calculated for all 1%-centrality intervals is shown. Up to 50%-centrality, that the ratios deviate less than 1% from 1. Above 70% the deviations rise above 10% going up to around 30% for ultra-peripheral collisions. The reason for such large deviations can perhaps be explained by the choice of different interpolation functions of the different codes. To extrapolate the (pseudo-) multiplicity distribution from the T<sub>R</sub>ENTo-output based histogram, one has to interpolate from the discrete histogram to a smooth interpolation function. Since the C++-based code relies on an interpolation function from the GNU-scientific library and the calculation in python uses an interpolation function from the SciPy library, these functions may differ, leading to those differences. Nevertheless, we will only investigate collisions of up to 40% centrality in this thesis, a centrality region where both codes produce reasonably equal results for our purposes.

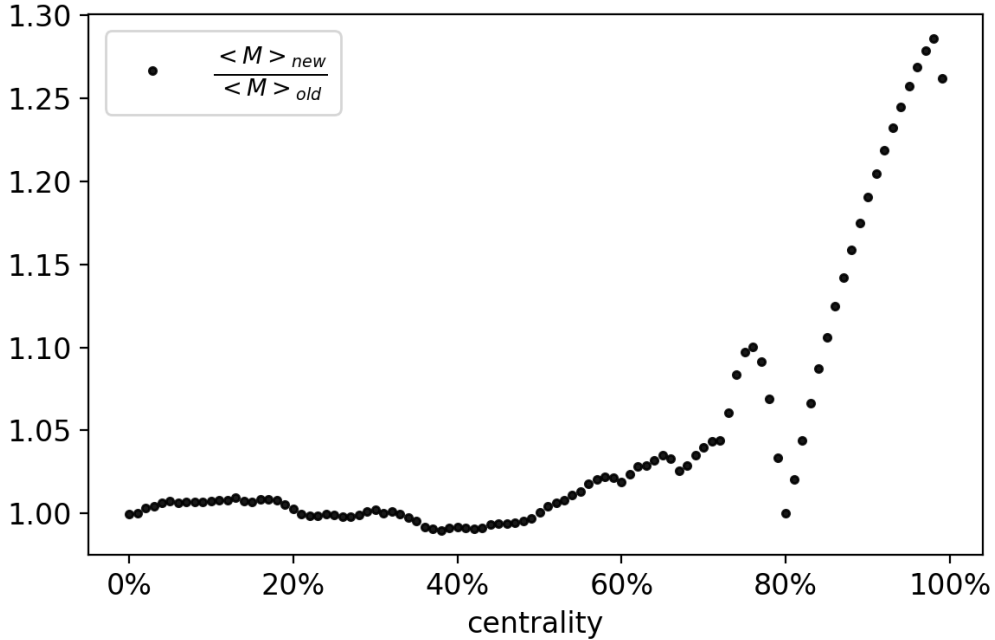


Figure 5.2: Ratio  $\langle M \rangle_{new} / \langle M \rangle_{old}$  as a function of centrality.  $\langle M \rangle_{new}$  denotes the averaged pseudo-multiplicity determined via a python routine determined within this thesis;  $\langle M \rangle_{old}$  denotes the same quantity determined via a C++ routine [31].

Secondly, we calculated  $\frac{dN}{dy}(|y| < 0.5)$  using the same version of FluiduM, as well as the same decay-kernels as in [24] but again our implementation of the initial condition calculation as discussed in **Section 5.2**. The sets of T<sub>R</sub>ENTo- and FluiduM model parameters are listed in the Tables 5.1. The comparison is illustrated in Fig. 5.3. The plot shows the ratio  $\frac{dN}{dy}_{new} / \frac{dN}{dy}_{old}$  as a function of centrality, for charged hadrons ( $h^+$ , blue) as well as for kaons ( $K^+$ , green), pions ( $\pi^+$ , yellow) and protons ( $p$ , red). Ideally, the ratio of all those values should be 1 since this would mean, that the calculation of the initial conditions as described in **Section 5.2** does not influence the final number of identified hadrons calculated by FluiduM. As one can see in Fig. 5.3, the maximal deviation between both set-ups is below 0.5%, which quantitatively justifies the determination of initial conditions as presented in **Section 5.2**.

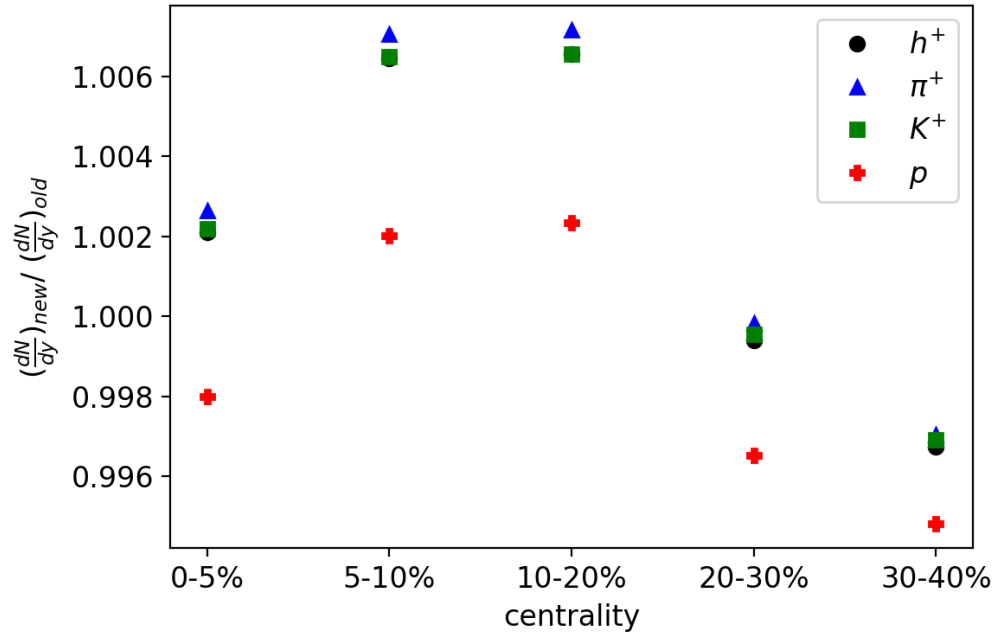


Figure 5.3: Ratios of the  $p_T$ -integrated particle yield (charged, pions, kaons and protons) at mid-rapidity determined with new initial conditions over the same quantity but calculated with initial conditions as used in [24].

# Chapter 6

## Systematic study of T<sub>R</sub>ENTo initial conditions for Pb-Pb collisions at $\sqrt{s_{NN}} = 2.76$ TeV and 5.02 TeV

### 6.1 Motivation

From what is known about the pre-equilibrium phase right after the collision, one can assume that the initial entropy density in the transverse plane at time  $\tau_0$  does depend on the energy of the colliding nuclei but *not* on the centrality of the event. Thus, it is expected that the *Norm* of the averaged initial entropy density profile (see Eq. 5.6) is universal for all events at a fixed collision energy. Ideal initial condition models are expected to reflect this aspect. In contrast, in the model-to-data fit analysis in [24] five different normalizations were allowed, varying for each centrality class, in order to reproduce experimental data accurately with the fit. Thus, the five best-fit values for the *Norm* obtained from the subsequent model-to-data fits analysis, varied over the centrality classes. As an initial condition model T<sub>R</sub>ENTo was used in [24].

The work presented in this thesis aims at approaching the centrality dependence of the normalization of the initial entropy density profile. Therefore, we examine Pb-Pb collisions at energies per nucleon pair of  $\sqrt{s_{NN}} = 2.76$  TeV and 5.02 TeV. The parametrization of the initial state description in T<sub>R</sub>ENTo is optimized by varying the value of  $p$  (see Eq. 4.10). To quantify our findings, we compare the particle multiplicity per unit rapidity at mid-rapidity  $\frac{dN}{dy}(|y| < 0.5)$  for five different centrality classes calculated by FluiduM and measured by the ALICE experiment.

## 6.2 Experimental data and uncertainties

For the model-to-data comparison of  $\frac{dN}{dy}$ , we used experimental results from ALICE. This study focuses on collisions of  $^{208}\text{Pb}$  ions at  $\sqrt{s_{NN}} = 2.76$  TeV and 5.02 TeV. In order to separate correlated from uncorrelated systematic uncertainties for experimentally measured values of  $\frac{dN}{dy}$ , we however refer to information on the correlation of uncertainties reported for  $\frac{dN_{ch}}{d\eta}$  of all charged particles at  $\sqrt{s_{NN}} = 2.76$  TeV. The reasons for that are explained in **Subsection 6.2**. For charged particle  $\frac{dN_{ch}}{d\eta}$  is not reported by ALICE.

Experimentally, the charged particle pseudorapidity density  $\frac{dN}{d\eta}$  (at mid-rapidity) is determined based on the analysis of signals from mainly two detectors, the Silicon Pixel detector (SPD) (two cylindrical layers of hybrid silicon pixel detectors around the beam-line) and the VZERO detector (two arrays of scintillator tiles with full azimuthal coverage in the longitudinal direction on either side of the Interaction Point). Based on the signal of the VZERO detector and MC Glauber simulations as well as further model assumptions on the particle production, centrality classes are defined [34]. The charged particle multiplicity density is then determined for each centrality class. They have significant systematic uncertainties, while statistical uncertainties are negligible. Data of  $\frac{dN_{ch}}{d\eta}$  at  $\sqrt{s_{NN}} = 2.76$  TeV was taken from [34].

For Pb-Pb collisions at  $\sqrt{s_{NN}} = 2.76$  TeV, the systematic uncertainties on  $\frac{dN_{ch}}{d\eta}$  are stated to be 3.7% for the most central collisions (0-5% centrality) and 7.0% for the most peripheral collisions (70-80% centrality) for charged particles. Large parts of these systematic uncertainties are correlated among centrality classes. A large part of that comes from the actual centrality class definition. For the 0-5% class the total correlated systematic uncertainty is stated to be 2.5%. So 67.6% of the total systematic uncertainty is correlated and 32.4% is uncorrelated. For the 70-80% centrality class, the total correlated systematic uncertainty is 5%. This amounts to a correlated part of 71.4% of the total systematic uncertainty and an uncorrelated part of 28.6%.

For all other centrality classes, the correlated systematic uncertainty was not explicitly stated in [34] and the respective analysis note. In order to treat uncorrelated and total systematic uncertainties of  $\frac{dN_{ch}}{d\eta}$  separately, a linear interpolation was applied to the previously stated values. Therefore, it was assumed that correlated and uncorrelated systematic uncertainty summed linearly are equal to the total systematic uncertainty of  $\frac{dN_{ch}}{d\eta}$ . A linear relationship between the uncorrelated (and also the correlated) part of the systematic uncertainties as a function of centrality was implied. In Fig. 6.1, the uncorrelated part of the systematic uncertainty (in percentage of the total systematic uncertainty) as a function of centrality is depicted. Furthermore, for identified particles, namely for  $\pi^{+/-}$ ,  $K^{+/-}$  and  $p, p^-$ , we assume, in this thesis, that the percentage of uncorrelated systematic uncertainty per centrality class is the same

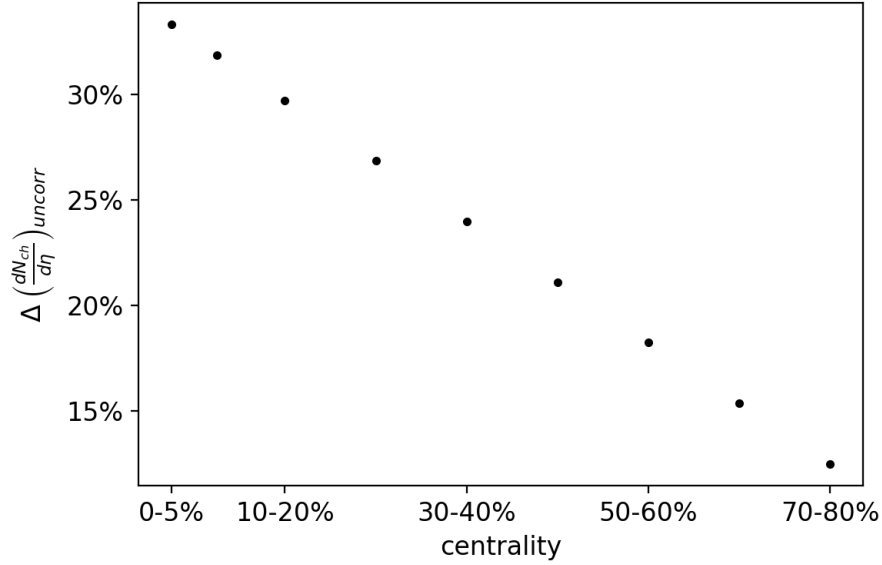


Figure 6.1: Relative uncorrelated systematic uncertainty on  $\frac{dN_{ch}}{d\eta}$  in percent as a function of centrality based on data from charged particles. Since [34] only states relative uncorrelated uncertainties for 0-5% and 70-80% centrality, the values for the centrality classes in between are obtained from a linear interpolation of the form  $y = a * x + b$ .

as for all charged particles. Data for identified charged particles at  $\sqrt{s_{NN}} = 2.76$  TeV and 5.02 TeV was taken from [35] and [36]. For a more rigorous approach, one would have to consider additional systematic uncertainties coming from particle identification. This separation of systematic uncertainties was only applied to data of Pb-Pb collisions at  $\sqrt{s_{NN}} = 2.76$  TeV.

## Rapidity vs. Pseudorapidity

Complications arise from the fact that for all charged hadrons ALICE data for values of  $\frac{dN_{ch}}{d\eta}$  at mid-pseudorapidity are reported in [34]. However, FluiduM does calculate  $\frac{dN}{dy}$  at mid-rapidity for charged particles at the moment. A conversion between  $\frac{dN_{ch}}{d\eta}$  and  $\frac{dN}{dy}$  requires knowledge of the exact particle composition of all charged particles detected by ALICE, since the conversion factor depends on the mass of the converted particle. In Fig. 6.2 an approximation for  $\frac{dN}{dy}$  for all charged particles measured in events with 0-5% centrality is depicted (on the right) as well as  $\frac{dN_{ch}}{d\eta}$  for different centrality classes (on the left). The figure shows results from Pb-Pb collisions measured by ALICE for  $\sqrt{s_{NN}} = 2.76$  TeV. At mid-rapidity ( $|\eta| < 0.5$  and  $|y| < 0.5$ ), the distributions are approximately constant, but differ substantially in absolute value. At 0-5% centrality the difference in absolute values of both distributions is  $\approx 200$ , more than 10% of  $\frac{dN_{ch}}{d\eta}$  in the respective mid-(pseudo-)rapidity range. Due to that fact, a comparison of  $\frac{dN_{ch}}{dy}$  from FluiduM and  $\frac{dN_{ch}}{d\eta}$  from ALICE data for all charged particles is not reasonable.

However, the total number of charged particles measured by ALICE consists predominately of pions, kaons and protons (and respective anti-particles) (above 95%) [37]. In FluiduM, the total multiplicity is for  $\approx 97\%$  equal to the sum of pions, kaons and protons (and respective antiparticles). For these particles, ALICE also reports values for the  $p_T$ -integrated yields  $\frac{dN}{dy}$  as a function of centrality (see [35, 36]). A comparison between ALICE data and FluiduM output is possible for these species. In order to make that comparison for all charged particles as well, in this thesis we therefore denote the sum of  $K^+$ ,  $K^-$ ,  $\pi^+$ ,  $\pi^-$ ,  $p$ , and  $p^-$  as **all charged particles** in context of FluiduM and ALICE data. We note that the separation of uncorrelated and correlated systematic uncertainty is based on  $\frac{dN_{ch}}{d\eta}$  measured in ALICE for all charged particles, but applied to measurements of  $\frac{dN}{dy}$  for pions, protons and kaons (as well as their sum). This inconsistency should be addressed in further studies.

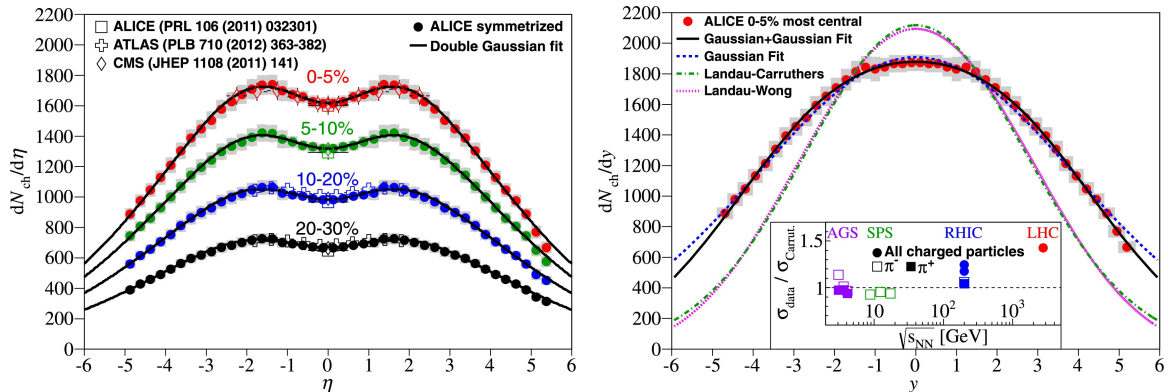


Figure 6.2: The left picture shows charged particle multiplicity distribution as a function of pseudorapidity measured by ALICE for Pb-Pb collisions at  $\sqrt{s_{NN}} = 2.76$  TeV. The measurements from ALICE in the 0-5% centrality class are indicated by the red points. The figure on the right shows an estimate of the respective charged particle multiplicity distribution as a function of rapidity  $y$  for 0-5% centrality. Again, the red points indicate ALICE data. (Figure taken from [38].)

## 6.3 Fits and Results

### 6.3.1 Analysis and Fits

In this section, we present the results of the study of the T<sub>R</sub>ENTo initial conditions within the simulation of Pb-Pb collisions at  $\sqrt{s_{NN}} = 2.76$  TeV and 5.02 TeV together with the FluiduM package. Its implementation was introduced in the previous chapter. In another work it was stated that initial conditions of Pb-Pb collisions are best described by setting the parameter  $p = 0$  in T<sub>R</sub>ENTo [27]. For our studies we calculated initial conditions with our T<sub>R</sub>ENTo implementation (see in **Section 4.3**) for  $p = -0.05, 0, 0.01, 0.05, 0.1, 0.2, 0.5$ . Subsequently, for each value of  $p$ ,  $\frac{dN}{dy} (|y| < 0.5)$  was calculated for the centrality classes 0-5%, 5-10%, 10-20%, 20-30%, 30-40% in FluiduM and compared to the respective ALICE data. In order to do so, we calculated the model-to-data ratio,

$$\frac{\left(\frac{dN}{dy}\right)_{Model}(p)}{\left(\frac{dN}{dy}\right)_{Data}} \quad (6.1)$$

for each of the five centrality classes. Since uncertainties are only given for the experimental data, the equation for the uncertainty of the ratio is:

$$\Delta \left( \frac{\left(\frac{dN}{dy}\right)_{Model}}{\left(\frac{dN}{dy}\right)_{Data}} \right) = \left( \frac{\left(\frac{dN}{dy}\right)_{Model}}{\left(\frac{dN}{dy}\right)_{Data}^2} \right) * \Delta \left( \frac{dN}{dy} \right)_{Data} \quad (6.2)$$

Ideally, the ratio would be one within the margins of the uncertainties for charged particles as well as for pions, kaons and protons. This would indicate an ideal agreement between experimental data and the theoretical model calculations. Furthermore, for a complete combined initial conditions and hydrodynamic model, that describes particle production accurately, we assume that there is no centrality dependence of these ratios. For a quantitative evaluation of the ratios for different values of  $p$ , we applied a linear fit of the form

$$y_{fit} = a * x + b \quad (6.3)$$

and evaluated the fit-parameters as well as the goodness of the fit. The latter is quantified by the  $\chi_{red}^2$  which is evaluated via

$$\chi_{red}^2 = \frac{1}{N_{DOF}} \sum_{i=1}^N \frac{(x_i - y_{fit,i})^2}{\sigma_{x_i}^2} \quad (6.4)$$

where  $N_{DOF}$  denotes the number of degrees of freedom, in this case  $5 - 2 = 3$ . The sum runs over the number of points of measurement. The variable  $x_i$  denotes the measured value, in our case the model-to-data ratio (Eq. 6.1) and  $\sigma_{x_i}$  the respective uncertainty (Eq. 6.2), while  $y_{fit,i}$  denotes the respective fit value. The results are presented in the following sections. For completeness, the T<sub>R</sub>ENTo parameters are listed in table 6.1.

For this study, we assumed a centrality independent normalization of the initial entropy density profile. The subsequent FluiduM-model parameters used here were taken from a unpublished study alongside the work of [24] using a similar global fit-procedure as for the best-fit values presented and explained in that paper. However, the  $\chi_{red}^2$  of the subsequent fit of the  $p_T$ -spectra lies at 1.47 in comparison to  $\chi_{red}^2 = 1.37$ , if a centrality independence of the *Norm* is assumed [24].

### 6.3.2 Fit results: Pb-Pb collisions at $\sqrt{s_{NN}} = 2.76$ TeV

First of all, one has to investigate the the model-to-data ratios for Pb-Pb collisions at  $\sqrt{s_{NN}} = 2.76$  TeV for  $p = 0$ . As previously mentioned, such a set-up was used for the analysis in [24] since it was stated in [27] that  $p = 0$  fits data from Pb-Pb collisions best. In Fig. 6.3, the model-to-data ratios as a function of centrality for  $p = 0$  for all charged particles, pions, kaons and protons are shown. The uncertainties on the points correspond only to the uncorrelated uncertainties. Assuming an complete theoretical model (hydrodynamic plus initial conditions plus freeze-out) in agreement with experimental data, one would expect a ratio of one. Furthermore, the model-to-data multiplicity ratios would ideally not depend on centrality hence a flat linear fit would describe the data perfectly. For protons, the model-to-data

<b>T<sub>R</sub>ENTo parameters</b>		<b>FluiduM parameters</b>	
projectiles	Pb-Pb	<i>Norm</i>	55.25/76.9
number of events	10 <sup>5</sup>	$\tau_0$ [fm c <sup>-1</sup> ]	0.179
reduced thickness parameter ( <i>p</i> )	-0.05, 0, 0.01, 0.05 0.1, 0.2, 0.5	$\eta/s$	0.166
fluctuation ( <i>k</i> )	1.4	$(\zeta/s)_{max}$	0.06
nucleon-width( <i>w</i> ) [fm]	0.6	$T_{fo}$ [MeV]	137
$\sigma_{NN}^{inel}$ [fm <sup>2</sup> ]	6.4/ 7.0	$p_T$ -range [GeV c <sup>-1</sup> ]	0-3.5 (in steps of 0.1)
normalization	1		
grid-max [fm]	10		
grid-step [fm]	0.2		

Table 6.1: Table showing the model parameters that were used for the analysis of Pb-Pb collisions at  $\sqrt{s_{NN}} = 2.76$  TeV and 5.02 TeV (for the latter colored in blue if differing). The meaning of the parameters is explained in the text and in the previous chapters.

ratio varies around 1. For kaons, the ratio varies around 1.06, which means that within the theoretical model, too many particles are produced in comparison to the number of experimentally measured kaons. On the other hand, the ratio of pion multiplicity densities varies around 0.8. Quantitatively between 15-20% more pions are measured than predicted by the theoretical model. This result agrees with results that were found in e.g. investigations of transverse momentum spectra of pions in [24]. At the low  $p_T$ -range an excess of pions is measured experimentally compared to what is expected from the current implementations of the theoretical models. This strongly indicates that the theoretical model description used in [24] is not complete but theoretical explanations exist that aim to explain the low- $p_T$  pion excess in terms of non-thermal production mechanisms or by the impact of resonance decays. Since pions are the most abundant particle species of all measured charged particles in heavy-ion collisions, this has to be considered also for the evaluation of the fits in this work. As one can see for all charged particles (which is in our case only the sum of charged pions, kaons and protons) the model-to-data ratio varies around 0.87 which strongly reflects the pion excess at low  $p_T$ .

The actual fits and their parameters for Pb-Pb collisions at  $\sqrt{s_{NN}} = 2.76$  TeV are presented in Fig. 6.4 - 6.6.

The four plots in Fig. 6.4 show the model-to-data ratios of  $\frac{dN}{dy}$  as a function of centrality for  $p = -0.05, 0, 0.01, 0.05$  of the T<sub>R</sub>ENTo initial conditions (shown in different colors). In Fig. 6.5 show the same quantities but for  $p = 0, 0.1, 0.2, 0.5$ . For visibility,

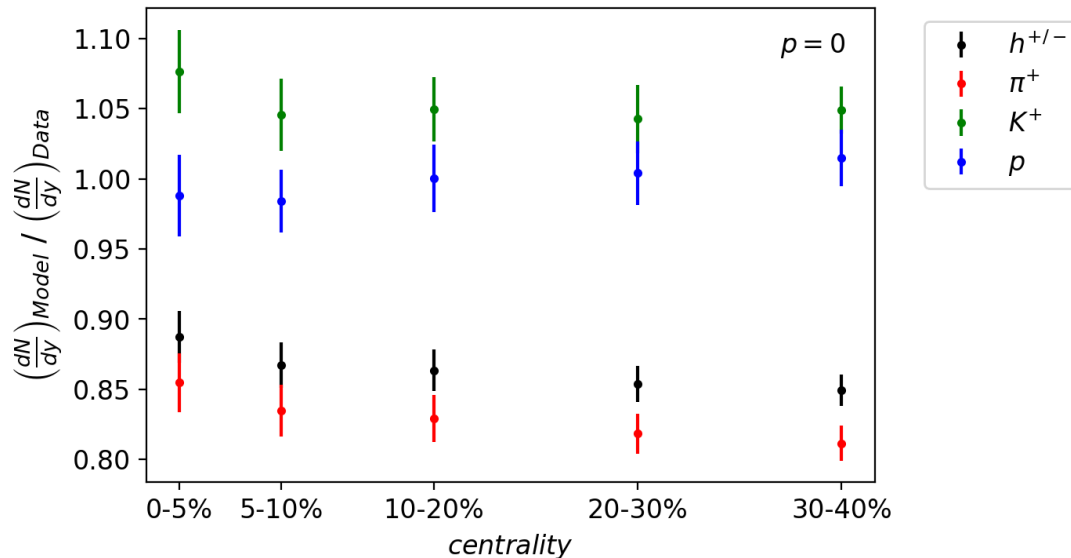


Figure 6.3: Model-to-data ratio of  $\frac{dN}{dy}$  (at mid rapidity) for all charged hadrons (black), pions (red), kaons (green) and protons (blue) calculated with FluiduM and T<sub>R</sub>ENTo initial conditions for  $p = 0$  compared to ALICE data. The depicted uncertainties correspond to the uncorrelated part of the uncertainty on the ratios. For details on the separation of the uncertainties, we refer to **Section 6.2**.

the points in each centrality class, that correspond to different values of  $p$ , are shifted horizontally. In each plot, the correlated systematic uncertainties are separated from the overall systematic uncertainty as described in **Section 6.2**. The total systematic uncertainties are represented in the background of each point by larger more transparent bars. The uncorrelated systematic uncertainties are represented by colored bars in the front. For the fit, only the uncorrelated systematic uncertainties were considered as errors. The fits were performed in python by using the `scipy.optimize.curve_fit`-function and the fit-function defined in Eq. 6.3.

For the evaluation of the linear fits, it has to be stressed that they are only applied to 5 data points (one for each centrality class), which restricts the significance of predictions based only on these fit-parameters. However, we used linear fits in order to additionally quantify visible trends of the model-to-data ratios. The fits are applied based on our assumption that the centrality dependence of the model-to-data ratios is mainly determined by the value of  $p$  of the T<sub>R</sub>ENTo-model, hence the parametrization of the initial entropy density profile. In Fig. 6.4 and Fig. 6.5, the fits applied had the slope  $a$  and the offset  $b$  of the linear function as free parameters. Their fit

parameters are listed in tables 6.2-6.5. Furthermore, the slope  $a$  as well as the offset  $b$  of the fit-function as a function of the  $p$ -value are shown in 6.6. For all fits  $\chi_{red}^2 < 1$ . That indicates that the data is over-fitted most probably due to the large systematic uncertainties on experimental measurements of  $\frac{dN}{dy}$ .

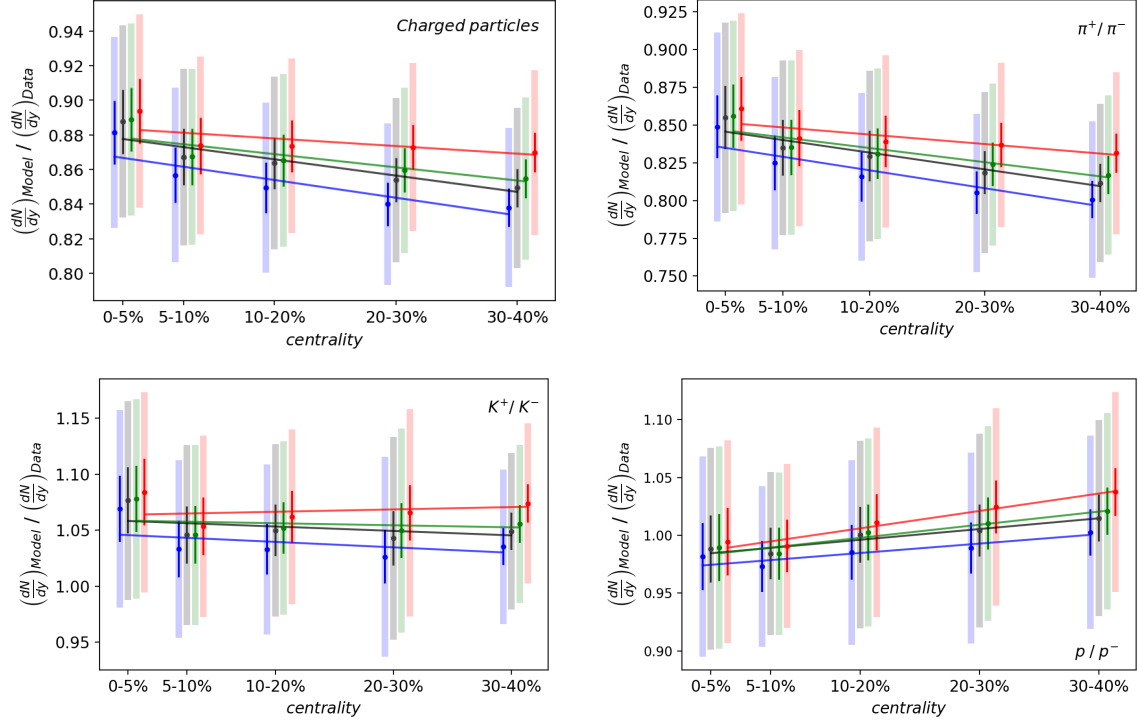
First of all, the plots and correspondingly the fit parameters show that we observe different trends for different particles. The slope of the fitted curves for kaons and charged particles for different values of  $p$  agree with each other. For pions the slopes of the fits for  $p = -0.05, 0, 0.01, 0.05$  are all negative, while for protons all slopes for the same values of  $p$  are positive. However, one can observe in all four cases that for increasing values of  $p$ , the slope of the fitted curves increases. This means that increasing  $p$  to values up to 0.1, 0.2 and further, worsens the model-to-data agreement significantly. Since we initially expected that varying the value of  $p$  in T<sub>R</sub>ENTo could increase the agreement of the theoretical results and the ALICE-data of  $\frac{dN}{dy}$ , we mainly assess the fits based on the flatness of the curves. A slope of zero would therefore indicate good agreement of model and data. We neglect charged particle and pion results for the interpretation. As we stressed earlier, they are largely influenced by the measured pion excess at low- $p_T$  which is present in all centrality classes. Furthermore the centrality dependence of the low- $p_T$  pion excess is not fully understood from the physics point of view. Including the results of our investigation for pion and all charged particle into the interpretation might lead to false conclusions concerning the description of the initial state and its centrality dependence.

Due to the large fit uncertainties for kaons, a result compatible with a flat behaviour ( $a = 0$ ) agrees with the ideal fit parameters of the curves for  $p = -0.05, 0, 0.01$  and  $0.05$  within their fit uncertainties. For all of these fits,  $\chi_{red}^2 \approx 0.03-0.05$  which again strongly indicates over-fitting of the data. For kaons at 0-5% centrality, the ratios for all values of  $p$  indicate a larger overproduction of kaons than for the rest of the centrality classes. This instance might be due to differences in the interpolation methods of  $p_T$ -spectra of  $p_T \rightarrow 0$  between the FluidUM calculation and the interpolation applied to experimental data.

Judging by the slope parameters from the proton fits, a slope of  $a = 0$  does not agree within the uncertainties with any of the fits for different  $p$ -value. The parameters indicate that possibly  $p < -0.05$  could further flatten the slopes of the proton ratios. For the proton fit, the  $\chi_{red}^2$  is on the order of 0.1 except for  $p = -0.05$  where  $\chi_{red}^2 = 0.006$ . In comparison to the kaon fits, the goodness of the fits for proton marginally improves, but still largely indicates over-fitting.

In conclusion, investigating the model-to-data ratio of  $p_T$ -integrated yields of charged particles produced in Pb-Pb collisions at  $\sqrt{s_{NN}} = 2.76$  TeV using the methods proposed in this thesis, does not lead to a general conclusion of *one* statistically

significant value for the parameter  $p$  in T<sub>R</sub>ENTo. Judging by linear fits to model-to-data ratios for protons and kaons one rather can limit the range of  $p$  with good agreement (for both particle species) possibly to  $p = (0 \pm 0.05)$ . However, one could consider further investigations in the same manner for  $p$ -values below  $p = -0.05$  to achieve improved agreement with protons. This result generally confirms the T<sub>R</sub>ENTo initial condition configuration in terms of the value of  $p$  that was used for the work in [24] and is consistent with the results from other work with T<sub>R</sub>ENTo as e.g. presented in [39]. However, the fit results pose some open questions, which are addressed in **Section 6.4**.



Legend:

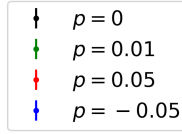


Figure 6.4: Model-to-data ratios of  $\frac{dN}{dy}$  as a function of centrality for Pb-Pb collisions at  $\sqrt{s_{NN}} = 2.76$  TeV for values of  $p = -0.05, 0, 0.01, 0.05$  indicated by different colors. A linear fit-function is applied to each set of points for one value of  $p$  and shown in the plot. The ratios are determined for all charged particles (see note in Subsection 6.2) and pions, kaons and protons, individually. The larger, shadowed bars in the back of each point show the total uncertainty based on the total systematic uncertainty of the ALICE data. The points in the front show the uncorrelated part of the uncertainty. For visibility, the points are shifted horizontally.

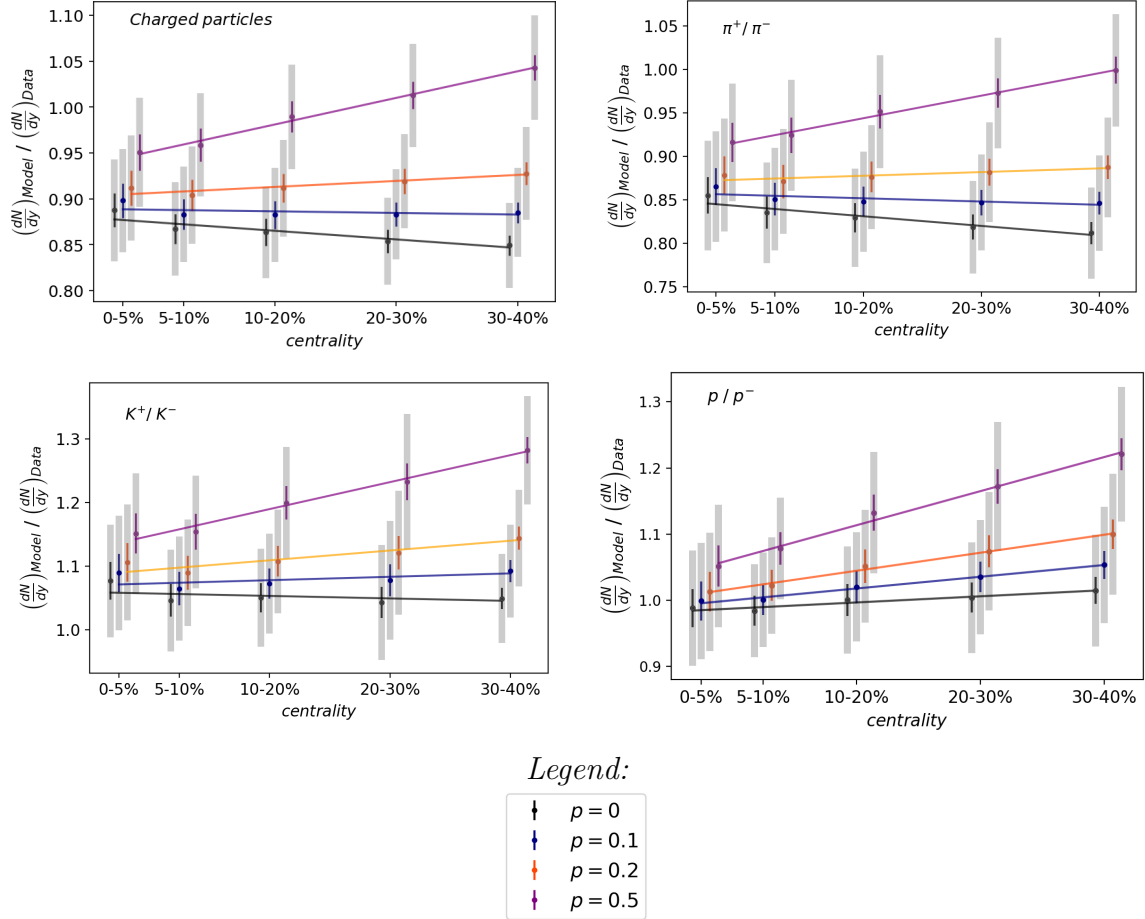


Figure 6.5: Model-to-data ratios of  $\frac{dN}{dy}$  as a function of centrality for Pb-Pb collisions at  $\sqrt{s_{NN}} = 2.76$  TeV for values of  $p = 0, 0.1, 0.2, 0.5$  indicated by different colors. The results are presented for the same particles as in Fig. 6.4. Total and uncorrelated uncertainties are presented in the same way as described in the text.

$p$	$a [10^{-4}]$	$b - 1 [10^{-2}]$	$\chi_{red}^2$	$p$	$a [10^{-4}]$	$b [10^{-2}]$	$\chi_{red}^2$
0	$-9.4 \pm 2.2$	$-12.0 \pm 0.5$	0.17	0	$-11.1 \pm 2.0$	$84.8 \pm 0.5$	0.11
0.01	$-7.6 \pm 2.4$	$-12.0 \pm 0.6$	0.20	0.01	$-9.4 \pm 2.2$	$84.8 \pm 0.5$	0.13
0.05	$-4.4 \pm 2.4$	$-11.6 \pm 0.6$	0.20	0.05	$-6.3 \pm 2.2$	$85.2 \pm 0.5$	0.13
-0.05	$-10.2 \pm 3.1$	$-13.0 \pm 0.8$	0.35	-0.05	$-11.9 \pm 2.9$	$83.9 \pm 0.7$	0.24
0.1	$-1.8 \pm 2.1$	$-11.1 \pm 0.5$	0.15	0.1	$-3.7 \pm 1.9$	$85.7 \pm 0.5$	0.10
0.2	$6.6 \pm 1.5$	$-9.6 \pm 0.4$	0.007	0.2	$4.2 \pm 1.3$	$87.1 \pm 0.3$	0.04
0.5	$29.0 \pm 1.3$	$-5.8 \pm 0.3$	0.46	0.5	$25.9 \pm 1.1$	$90.8 \pm 0.3$	0.03

Table 6.2: Fit parameters for charged particles

Table 6.3: Fit parameters for  $\pi^+/\pi^-$

$p$	$a [10^{-4}]$	$b - 1 [10^{-2}]$	$\chi_{red}^2$	$p$	$a [10^{-4}]$	$b [10^{-2}]$	$\chi_{red}^2$
0	$-3.9 \pm 4.0$	$5.9 \pm 1.0$	0.03	0	$9.3 \pm 1.6$	$98.2 \pm 0.3$	0.07
0.01	$-1.8 \pm 4.2$	$5.9 \pm 1.0$	0.04	0.01	$11.3 \pm 1.8$	$98.2 \pm 0.4$	0.09
0.05	$2.1 \pm 4.2$	$6.4 \pm 1.0$	0.04	0.05	$15.1 \pm 1.8$	$98.5 \pm 0.4$	0.13
-0.05	$-4.9 \pm 5.0$	$4.7 \pm 1.2$	0.05	-0.05	$8.1 \pm 2.0$	$97.2 \pm 0.4$	0.006
0.1	$5.4 \pm 3.9$	$7.0 \pm 1.0$	0.017	0.1	$17.8 \pm 1.2$	$99.1 \pm 0.3$	0.08
0.2	$15.4 \pm 3.3$	$8.7 \pm 0.8$	0.022	0.2	$27.3 \pm 1.4$	$100.6 \pm 0.3$	0.23
0.5	$42.5 \pm 2.8$	$13.2 \pm 0.6$	0.08	0.5	$51.6 \pm 2.8$	$104.3 \pm 0.6$	0.69

Table 6.4: Fit parameters for  $K^+ / K^-$

Table 6.5: Fit parameters for  $p / \bar{p}$

Fit parameters and  $\chi_{red}^2$  for fits to all charged particles, pions, kaons and protons from model-to-data ratios of  $\frac{dN}{dy}$  of Pb-Pb collisions at  $\sqrt{s_{NN}} = 2.76$  TeV.

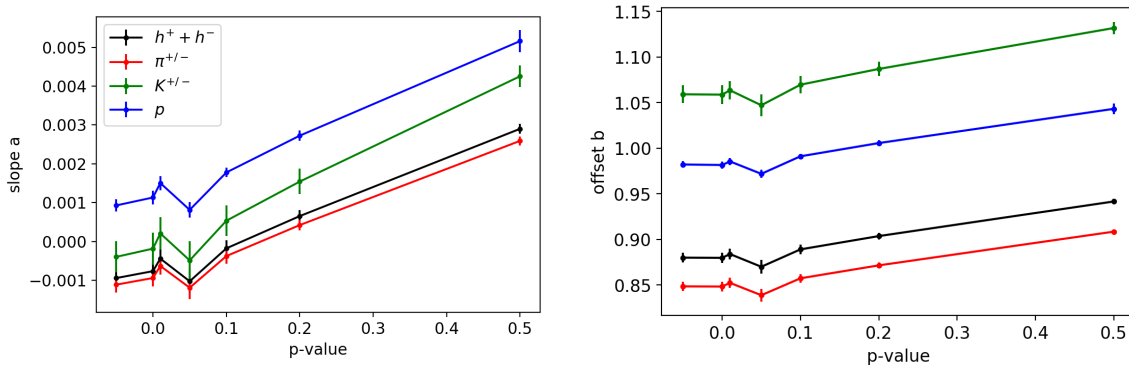


Figure 6.6: Fit-results combined for all model-to-data comparisons for Pb-Pb collisions at  $\sqrt{s_{NN}} = 2.76$  TeV depicted graphically. The left plot shows the slopes of the fit-functions as a function of  $p$  for the different particle species. On the right the offset  $b$  of the linear fit-function as a function of  $p$  is shown. The colors in both graphs are the same as indicated by the legend. In both cases the connection between the points is made for better visibility *without* an underlying assumption on a function that describes the dependence of the fit-parameters on  $p$ .

### 6.3.3 Comparison of results: Pb-Pb collisions at $\sqrt{s_{NN}} = 5.02$ TeV

In addition, Pb-Pb collisions at  $\sqrt{s_{NN}} = 5.02$  TeV were investigated with a similar approach as for the lower energy case. At higher collision energies, the QGP created in the collision, is hotter than at  $\sqrt{s_{NN}} = 2.76$  TeV. In terms of FluiduM parameters, this manifests itself as a higher normalization constant of the initial entropy density profile. Furthermore the transport coefficients  $\eta/s$  and  $\zeta/s$  are actually temperature dependent quantities, but for the work in this thesis we assume the same values for the study at  $\sqrt{s_{NN}} = 5.02$  TeV as at  $\sqrt{s_{NN}} = 2.76$  TeV. The model parameters that were used are given in table 6.1 (colored in blue if the value differs from the one at  $\sqrt{s_{NN}} = 2.76$  TeV). However, the FluiduM parameters in this case are not constraint by fits of transverse momentum spectra as it was the case for  $\sqrt{s_{NN}} = 2.76$  TeV. For a more reliable results one would first have to constrain the FluiduM model parameters by a fit routine as in [24] for  $\sqrt{s_{NN}} = 2.76$  TeV. The normalization constant of the entropy density, which acts as a scaling factor of the  $p_T$ -spectra in FluiduM, was adjusted in [24] such that for charged particles, the FluiduM data and ALICE measurements approximately agree. Consequently, the results for  $\sqrt{s_{NN}} = 5.02$  TeV can only predict the possible centrality dependence of integrated particle yields at mid-rapidities and their agreement within model and data for T<sub>R</sub>ENTo initial conditions with different values of  $p$ . Fig. 6.7, shows again the model-to-data ratio of  $p_T$ -integrated charged

particle yield  $\frac{dN}{dy}$  Pb-Pb collisions at  $\sqrt{s_{NN}} = 5.02$  TeV for different values of  $p$  in T<sub>R</sub>ENTo, indicated by different colors. Points for different values of  $p$  are shifted to improve the visualization. The errors shown are the systematic uncertainties of  $\frac{dN}{dy}$  extracted from ALICE measurements but not separated into correlated and uncorrelated systematic uncertainties as before. A linear fit is applied to model-to-data ratios. Due to the large total systematic uncertainties, all fits strongly over-fit the data such that no statistically significant statement on the slopes of the curves and a possibly preferred  $p$  can be made. The ratio points especially for protons show a different centrality dependence than for  $\sqrt{s_{NN}} = 2.76$  TeV, indicating that the value for  $p$  in T<sub>R</sub>ENTo might be a temperature/energy-dependent parameter. Looking at the slopes of the fitted curves to kaons and protons, one might conclude that a value for  $p \leq 0.05$  could improve the model-to-data agreement resulting in a flatter curve. Due to the large systematic uncertainties, this would have to be proven, by fitting again using only to the uncorrelated part of the uncertainty.

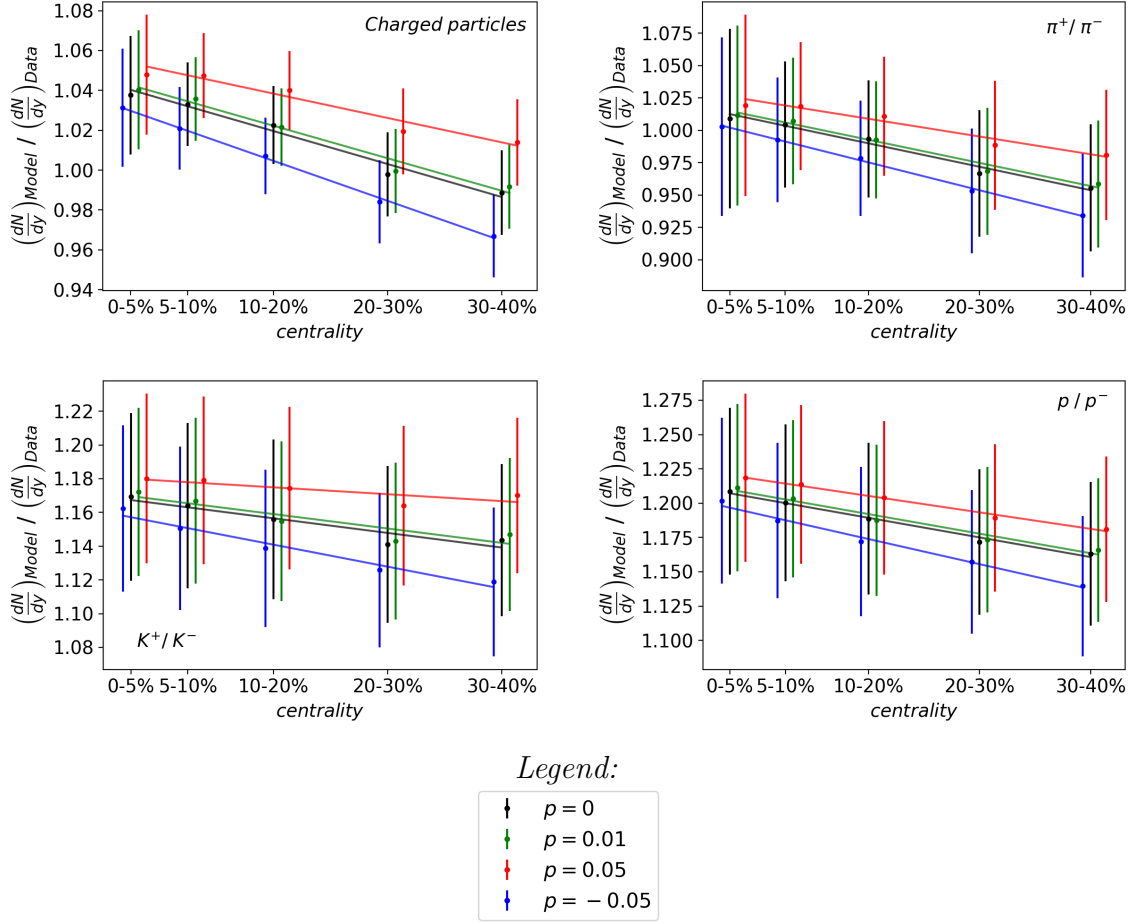


Figure 6.7: Model-to-data ratio of  $\frac{dN}{dy}$  as a function of centrality for Pb-Pb collisions at  $\sqrt{s_{NN}} = 5.02$  TeV for values of  $\rho = -0.05, 0, 0.01, 0.05$  shown in different colors. Linear fit-functions are indicated for all particle species. The uncertainty of each point corresponds to the total uncertainty, based on the total systematic uncertainty on ALICE data. For visibility the points are shifted horizontally.

### 6.3.4 Bugs in the code and possible error sources

Towards the end of the work of this thesis an error in the FluiduM Mathematica code was discovered. The error has a significant effect on the  $p_T$ -spectra as shown in Fig. 6.8. The effect of the error might influence the results of this thesis as well, since effectively the  $p_T$ -integrated spectra were examined. Since the best-fit parameter analysis in [24] was done with the same version of the FluiduM code, these values are also affected by the error in the code. Since new best-fit parameters determined with the corrected version of FluiduM were not available before the end of this thesis, we would suggest to do a similar analysis of initial conditions with corrected model parameters in case they vary significantly from the old ones.

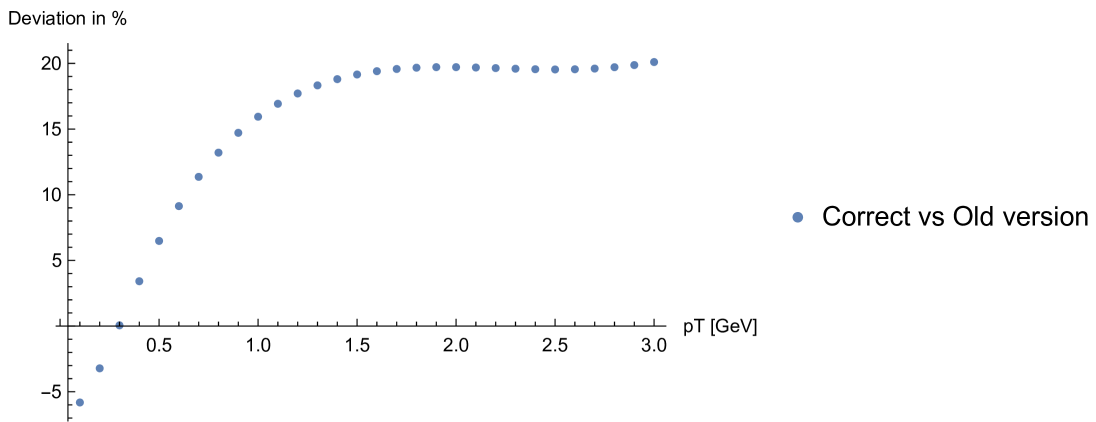


Figure 6.8: Deviation of  $p_T$ -spectra calculated with old FluiduM-version and with the new FluiduM version as a function of  $p_T$  for charged hadrons at 0-5%-centrality are shown. Picture courtesy of Daniel Boneß.

## 6.4 Open questions and further steps

The model-to-data ratios place open questions, that are not only concerning the initial condition description but also specifics on the implementation of FluiduM itself.

### Relative particle abundances

The comparison of the particle multiplicities from model and data showed that the FluiduM model does calculate a larger kaon abundance than what is measured by ALICE. This might be explained by the fact that the current implementation in FluiduM only features one freeze-out temperature and does not distinguish between

chemical and kinetic freeze-out. Therefore, future plans include an implementation of two freeze-out temperatures in FluiduM adjusting the equations of state in FluiduM accordingly.

### Initial conditions

The analysis proposed in this thesis, is not able to determine a statistically significant value for  $p$  in T<sub>R</sub>ENTo that improves agreement with experimental data. For confirmation of the range  $p = 0 \pm 0.05$  for Pb-Pb collisions at  $\sqrt{s_{NN}} = 2.76$  TeV determined based on the fit results, we propose to do a similar grid search as in [24]. Therefore one could use the same FluiduM model-parameters as in 6.1 but calculate  $p_T$ -spectra in FluiduM with initial conditions with a value of  $p$  within the proposed range. The value of  $\chi^2_{red}$  based on the fits of experimentally measured and calculated  $p_T$ -spectra for different particle species then indicates whether initial conditions calculated with a different value of  $p$  improves the model-to-data agreement.

Even further investigations could involve a similar systematic model-to-data comparison (as in this thesis) for a different variable with a higher sensitivity towards the initial state description. Possible candidates would be flow coefficients, since they depend on pressure anisotropies caused by the irregular shape and size of the initial entropy (or energy) density profile. This could possibly help constraining the value of  $p$  in T<sub>R</sub>ENTo to a narrower range. Furthermore such an investigation could resolve the issue why our data indicates that different particle species 'favor' different initial conditions as indicated by the differing kaon and proton slopes in Fig. 6.4 for  $\sqrt{s_{NN}} = 2.76$  TeV but not at  $\sqrt{s_{NN}} = 5.02$  TeV. The answer therefore is possibly not related to the initial condition description itself but some other aspect of the model, because a complete model would (most probably) not include different initial conditions for different particle species.

# Chapter 7

## Conclusion and Outlook

In this bachelor thesis, initial entropy density profiles at time of the thermalization of the QGP were calculated using the initial condition model T<sub>R</sub>ENTo for different values of  $p$  for a hydrodynamic simulation of heavy-ion collisions. A routine to calculate the averaged two-dimensional entropy density profiles already existed, though a new python routine was implemented in the course of this thesis to calculate the average multiplicity in 1%-centrality intervals.

In order to optimize the initial state description for simulated Pb-Pb collisions at  $\sqrt{s_{NN}} = 2.76$  TeV, theoretical calculations with the FluiduM package of the  $p_T$ -integrated particle yield  $\frac{dN}{dy}$  at mid-rapidity ( $|y| < |0.5|$ ) of pions, kaons and protons as well as charged particles were compared to ALICE data. The systematic uncertainty of the measurements were separated into uncorrelated and correlated uncertainty, such that for fits only the uncorrelated part of the systematic uncertainty was considered. The comparison was done for five centrality classes: 0-5%, 5-10%, 10-20%, 20-30% and 30-40%. For a quantitative comparison, the model-to-data ratio for different values of  $p$  as a function of centrality were fitted by a linear curve and fit-parameters as well as a  $\chi^2_{red}$ -value were obtained for each curve. Due to the impact of previously observed pion excess at low  $p_T$ , only the fit-results for protons and kaons are used in order to predict a range for  $p$  that improves the model-to-data agreement.

At  $\sqrt{s_{NN}} = 2.76$  TeV, it is not possible to determine one statistically significant value for  $p$  in T<sub>R</sub>ENTo due to large fit uncertainties. For  $p = 0 \pm 0.05$ , the kaon yield of the model agrees with ALICE data within the uncertainties. The proton-fit indicates that ALICE data might agree with model calculations for  $p < -0.05$  within the uncertainties of the model-to-data ratio. Furthermore, for  $p$  approaching 0.5 the agreement of model calculation and data becomes centrality dependent. For more peripheral collisions, the model produces significantly more particle than are measured experimentally. For  $\sqrt{s_{NN}} = 5.02$  TeV, the model-to-data ratios are reported too. Since FluiduM model parameters are not yet constraint by an underlying global fit

optimization, they are treated as first predictions for the model-to-data agreement with initial conditions in T<sub>R</sub>ENTo with different values of  $p$ . The uncertainties are not separated as before.

With the limitations of the fits in mind, we conclude that the approach chosen in this thesis, cannot constrain the value of  $p$  in T<sub>R</sub>ENTo to a narrow range around  $p = 0$  for Pb-Pb collisions at both collision energies. We propose a similar model-data-comparison but applied to flow coefficients  $v_n$  due to their high sensitivity to the shape and size of the initial transverse entropy density profile. Furthermore, it was discovered that the abundance of kaons calculated by the FluiduM model is significantly higher (around 6% for  $p = 0$ ) compared to what is measured by ALICE if only uncorrelated uncertainties are considered. A distinction between kinetic and chemical freeze-out in future work might take care of that difference. Due to an error in the implementation of the FluiduM code that was discovered towards the end of this thesis, its influence on the the FluiduM model parameter as well as the work of this thesis will have to be checked.

# Acknowledgments

First, I would like to say a big thank you to Prof. Dr. Silvia Masciocchi for giving me the opportunity to be part of her group and for the time she invested and her great effort on mentoring us students especially in these Corona times. Also, I would also like to thank the Isoquant C06-team, for the discussions that allowed me to get a deeper insight into the field of heavy-ion physics and for the help with my thesis. Thank you to Dr. Andrea Dubla for proofreading my thesis and Dr. Dhevan Gangadharan for helping me with questions and issues with my work. Finally, I would like to thank Benedikt Schosser for proofreading the final thesis.

# Bibliography

- [1] The ALICE Collaboration et al. “The ALICE experiment at the CERN LHC”. In: *Journal of Instrumentation* 3.08 (Aug. 2008), S08002–S08002. DOI: 10.1088/1748-0221/3/08/s08002. URL: <https://doi.org/10.1088%2F1748-0221%2F3%2F08%2Fs08002>.
- [2] Stefan Floerchinger, Eduardo Grossi, and Jorrit Lion. “Fluid dynamics of heavy ion collisions with mode expansion”. In: *Phys. Rev. C* 100.1 (2019), p. 014905. DOI: 10.1103/PhysRevC.100.014905. arXiv: 1811.01870 [nucl-th].
- [3] *Standard model of elementary particles: the 12 fundamental fermions and 5 fundamental bosons*. URL: [https://commons.wikimedia.org/wiki/File:Standard\\_Model\\_of\\_Elementary\\_Particles.svg#/media/File:Standard\\_Model\\_of\\_Elementary\\_Particles.svg](https://commons.wikimedia.org/wiki/File:Standard_Model_of_Elementary_Particles.svg#/media/File:Standard_Model_of_Elementary_Particles.svg). (accessed: 14.09.2020).
- [4] Bogdan Povh et al. *Teilchen und Kerne. Eine Einführung in die physikalischen Konzepte*. ger. 9. Aufl. 2014. SpringerLink : Bücher. Berlin, Heidelberg: Springer Spektrum, 2014, Online-Ressource (XII, 467 S. 160 Abb, online resource). ISBN: 978-3-642-37822-5. DOI: 10.1007/978-3-642-37822-5.
- [5] Mark Thomson. *Modern particle physics*. eng. Cambridge [u.a.]: Cambridge University Press, 2013, XVI, 554 S. ISBN: 978-1-107-03426-6 and 1-107-03426-4.
- [6] P.A. Zyla et al. (Particle Data Group). “Review of Particle Physics, Progress of Theoretical and Experimental Physics”. In: 2020.8 (August 2020), pp. 1–54. DOI: <https://doi.org/10.1093/ptep/ptaa104>.
- [7] *Heavy ions and quark-gluon plasma*. URL: <https://home.cern/science/physics/heavy-ions-and-quark-gluon-plasma>. (accessed: 18.09.2020).
- [8] Helmut Satz. “The Quark-Gluon Plasma – A Short Introduction”. In: *Nuclear Physics A* 862-863 (2011). The Sixth International Conference on Physics and Astrophysics of Quark Gluon Plasma (ICPAQGP-2010), pp. 4–12. ISSN: 0375-9474. DOI: <https://doi.org/10.1016/j.nuclphysa.2011.05.014>.

- [9] J. C. Collins and M. J. Perry. “Superdense matter: Neutrons or asymptotically free quarks?” In: 34.21 (May 1975), pp. 1353–1356. DOI: 10.1103/PhysRevLett.34.1353.
- [10] Johanna Stachel. “Flüssige Quarkmaterie”. In: Physik Journal (Juni 2005). DOI: <https://www.pro-physik.de/restricted-files/105321>.
- [11] K. Adcox et. al. (PHENIX Collaboration). “Formation of dense partonic matter in relativistic nucleus–nucleus collisions at RHIC: Experimental evaluation by the PHENIX Collaboration”. In: *Nuclear Physics A* 757.1 (2005). First Three Years of Operation of RHIC, pp. 184–283. ISSN: 0375-9474. DOI: <https://doi.org/10.1016/j.nuclphysa.2005.03.086>.
- [12] B.B. Back et. al. “The PHOBOS perspective on discoveries at RHIC”. In: *Nuclear Physics A* 757.1 (2005). First Three Years of Operation of RHIC, pp. 28–101. ISSN: 0375-9474. DOI: <https://doi.org/10.1016/j.nuclphysa.2005.03.084>.
- [13] Reinhard Stock. “Relativistic Nucleus-Nucleus Collisions and the QCD Matter Phase Diagram”. In: (July 2008). DOI: 10.1007/978-3-540-74203-6\_7. arXiv: 0807.1610 [nucl-ex].
- [14] Wit Busza, Krishna Rajagopal, and Wilke van der Schee. “Heavy Ion Collisions: The Big Picture and the Big Questions”. In: *Annual Review of Nuclear and Particle Science* 68.1 (2018), pp. 339–376. DOI: 10.1146/annurev-nucl-101917-020852.
- [15] A.K. Chaudhuri. *A short course on Relativistic Heavy Ion Collisions*. IOPP, Sept. 2014. ISBN: 978-0-7503-1061-1, 978-0-7503-1060-4. DOI: 10.1088/978-0-750-31060-4. arXiv: 1207.7028 [nucl-th].
- [16] Ulrich Heinz and Raimond Snellings. “Collective flow and viscosity in relativistic heavy-ion collisions”. In: *Ann. Rev. Nucl. Part. Sci.* 63 (2013), pp. 123–151. DOI: 10.1146/annurev-nucl-102212-170540. arXiv: 1301.2826 [nucl-th].
- [17] H.Masui. *Elliptic Flow*. URL: [http://utkhii.px.tsukuba.ac.jp/ATHIC2008/Talk\\_Slides\\_files/2C2-2\\_Masui.pdf](http://utkhii.px.tsukuba.ac.jp/ATHIC2008/Talk_Slides_files/2C2-2_Masui.pdf). (accessed: 23.09.2020).
- [18] Charles Gale, Sangyong Jeon, and Bjoern Schenke. “Hydrodynamic Modeling of Heavy-Ion Collisions”. In: *Int. J. Mod. Phys. A* 28 (2013), p. 1340011. DOI: 10.1142/S0217751X13400113. arXiv: 1301.5893 [nucl-th].
- [19] B. Alver and G. Roland. “Erratum: Collision-geometry fluctuations and triangular flow in heavy-ion collisions [Phys. Rev. C 81, 054905 (2010)]”. In: 82.3, 039903 (Sept. 2010), p. 039903. DOI: 10.1103/PhysRevC.82.039903.

- [20] L. Betev et. al. *Definition of the ALICE Coordinate System and Basic Rules for Sub-detector Components Numbering*. URL: <http://personalpages.to.infn.it/~tosello/EngMeet/NamingConventions/ALICE-INT-2003-038.pdf>. (accessed: 14.10.2020).
- [21] Sourav Sarkar, Helmut Satz, and Bikash Sinha. *The Physics of the Quark-Gluon Plasma. Introductory Lectures*. eng. Lecture notes in physics ARRAY(0x55a51d712638). Berlin, Heidelberg: Springer Berlin Heidelberg, 2009, pp. 29–38. ISBN: 978-3-642-02286-9. DOI: 10.1007/978-3-642-02286-9. URL: <http://dx.doi.org/10.1007/978-3-642-02286-9>.
- [22] Huichao Song and Ulrich Heinz. “Multiplicity scaling in ideal and viscous hydrodynamics”. In: *Phys. Rev. C* 78 (2 Aug. 2008), p. 024902. DOI: 10.1103/PhysRevC.78.024902. URL: <https://link.aps.org/doi/10.1103/PhysRevC.78.024902>.
- [23] Michael L. Miller et al. “Glauber Modeling in High-Energy Nuclear Collisions”. In: *Annual Review of Nuclear and Particle Science* 57.1 (Nov. 2007), pp. 205–243. ISSN: 1545-4134. DOI: 10.1146/annurev.nucl.57.090506.123020.
- [24] D. Devetak et al. “Global fluid fits to identified particle transverse momentum spectra from heavy-ion collisions at the Large Hadron Collider”. In: *JHEP* 06 (2020), p. 044. DOI: 10.1007/JHEP06(2020)044. arXiv: 1909.10485 [hep-ph].
- [25] Roy J. Glauber. “Quantum Optics and Heavy Ion Physics”. In: 774 (Aug. 2006), pp. 3–13. DOI: 10.1016/j.nuclphysa.2006.06.009. arXiv: nucl-th/0604021 [nucl-th].
- [26] H. De Vries, C.W. De Jager, and C. De Vries. “Nuclear charge-density-distribution parameters from elastic electron scattering”. In: *Atomic Data and Nuclear Data Tables* 36.3 (1987), pp. 495–536. ISSN: 0092-640X. DOI: [https://doi.org/10.1016/0092-640X\(87\)90013-1](https://doi.org/10.1016/0092-640X(87)90013-1). URL: <http://www.sciencedirect.com/science/article/pii/0092640X87900131>.
- [27] J. Scott Moreland, Jonah E. Bernhard, and Steffen A. Bass. “Alternative ansatz to wounded nucleon and binary collision scaling in high-energy nuclear collisions”. In: *Phys.Rev. C* 92.1 (2015), p. 011901. DOI: 10.1103/PhysRevC.92.011901. arXiv: 1412.4708 [nucl-th].
- [28] Piotr Bożek and Wojciech Broniowski. “Collective dynamics in high-energy proton-nucleus collisions”. In: 88.1, 014903 (July 2013), p. 014903. DOI: 10.1103/PhysRevC.88.014903. arXiv: 1304.3044 [nucl-th].
- [29] John Scott Moreland Jonah Bernhard. *Trento GitHub Code*. URL: <https://github.com/Duke-QCD/trento.git>. (accessed: 14.09.2020).

- [30] Steffen A. Bass, Jonah Bernhard, John Scott Moreland. *Trento Documentation*. URL: <http://qcd.phy.duke.edu/trento/index.html>. (accessed: 14.09.2020).
- [31] Kianusch Vahid Yousefnia. *Code for initial conditions in FluiduM*. URL: <https://github.com/kinuskia/Heavy-Ion-Collision-Analysis>. (accessed: 30.09.2020).
- [32] *Scipy Documentation*. URL: [https://docs.scipy.org/doc/scipy/reference/generated/scipy.stats.rv\\_histogram.html#scipy.stats.rv\\_histogram](https://docs.scipy.org/doc/scipy/reference/generated/scipy.stats.rv_histogram.html#scipy.stats.rv_histogram). (accessed: 30.09.2020).
- [33] Fred Cooper and Graham Frye. “Comment on the Single Particle Distribution in the Hydrodynamic and Statistical Thermodynamic Models of Multiparticle Production”. In: *Phys. Rev. D* 10 (1974), p. 186. DOI: 10.1103/PhysRevD.10.186.
- [34] Kenneth Aamodt et al. “Centrality dependence of the charged-particle multiplicity density at mid-rapidity in Pb-Pb collisions at  $\sqrt{s_{NN}} = 2.76$  TeV”. In: *Phys. Rev. Lett.* 106 (2011), p. 032301. DOI: 10.1103/PhysRevLett.106.032301. arXiv: 1012.1657 [nucl-ex].
- [35] Betty Abelev et al. “Centrality dependence of  $\pi$ , K, p production in Pb-Pb collisions at  $\sqrt{s_{NN}} = 2.76$  TeV”. In: *Phys. Rev. C* 88 (2013), p. 044910. DOI: 10.1103/PhysRevC.88.044910. arXiv: 1303.0737 [hep-ex].
- [36] Shreyasi Acharya et al. “Production of charged pions, kaons, and (anti-)protons in Pb-Pb and inelastic  $pp$  collisions at  $\sqrt{s_{NN}} = 5.02$  TeV”. In: *Phys. Rev. C* 101.4 (2020), p. 044907. DOI: 10.1103/PhysRevC.101.044907. arXiv: 1910.07678 [nucl-ex].
- [37] Anton Andronic et al. “Decoding the phase structure of QCD via particle production at high energy”. In: 561.7723 (Sept. 2018), pp. 321–330. DOI: 10.1038/s41586-018-0491-6. arXiv: 1710.09425 [nucl-th].
- [38] E. Abbas et al. “Centrality dependence of the pseudorapidity density distribution for charged particles in Pb–Pb collisions at  $s_{NN}=2.76$  TeV”. In: *Physics Letters B* 726.4 (2013), pp. 610–622. ISSN: 0370-2693. DOI: <https://doi.org/10.1016/j.physletb.2013.09.022>. URL: <http://www.sciencedirect.com/science/article/pii/S0370269313007399>.
- [39] Jonah E. Bernhard, J. Scott Moreland, and Steffen A. Bass. “Bayesian estimation of the specific shear and bulk viscosity of quark–gluon plasma”. In: *Nature Phys.* 15.11 (2019), pp. 1113–1117. DOI: 10.1038/s41567-019-0611-8.

# Erklärung

Ich versichere, dass ich diese Arbeit selbstständig verfasst und keine anderen als die angegebenen Quellen und Hilfsmittel benutzt habe.

Heidelberg, den 09.11.2020,

Y. Gieritz